Computational modeling of the nonlinear stochastic dynamics of horizontal drillstrings

Americo Cunha Jr, Christian Soize, Rubens Sampaio

Computational Mechanics manuscript No.
(will be inserted by the editor)

Computational modeling of the nonlinear stochastic dynamics of horizontal drillstrings

Americo Cunha Jr · Christian Soize · Rubens Sampaio

Received: date / Accepted: date

Abstract This work intends to analyze the nonlinear stochastic dynamics of drillstrings in horizontal configuration. For this purpose, it considers a beam theory, with effects of rotatory inertia and shear deformation, which is capable of reproducing the large displacements that the beam undergoes. The friction and shock effects, due to beam/borehole wall transversal impacts, as well as the force and torque induced by bit-rock interaction, are also considered in the model. Uncertainties of bit-rock interaction model are taken into account using a parametric probabilistic approach. Numerical simulations have shown that the mechanical system of interest has a very rich nonlinear stochastic dynamics, which generate phenomena such as bit-bounce, stick-slip, and transverse impacts. A study aiming to maximize the drilling process efficiency, varying drillstring velocities of translation and rotation is presented. Also, the work presents the definition and solution of two optimizations problems, one deterministic and one robust, where the objective is to maximize drillstring rate of penetration into the soil respecting its structural limits.

A. Cunha Jr (corresponding author)
Universidade do Estado do Rio de Janeiro, Instituto de Matemática e Estatística, Departamento de Matemática Aplicada, Rua São Francisco Xavier, 524, Pav. João Lyra, Bl. B, Sala 6032, Rio de Janeiro, 20550-900, Brasil
E-mail: americo@ime.uerj.br

A. Cunha Jr, C. Soize
Université Paris-Est, Laboratoire Modélisation et Simulation Multi Echelle, MSME UMR 8208 CNRS, 5, Boulevard Descartes 77454, Marne-la-Vallée, France
E-mail: christian.soize@univ-paris-est.fr

A. Cunha Jr, R. Sampaio
PUC–Rio, Departamento de Engenharia Mecânica, Rua M. de São Vicente, 225 - Rio de Janeiro, 22451-900, Brasil
E-mail: rsampaio@puc-rio.br

Keywords nonlinear dynamics · horizontal drillstring · uncertainty quantification · parametric probabilistic approach · robust optimization

1 Introduction

High energy demands of 21st century make that fossil fuels, like oil and shale gas, still have great importance in the energy matrix of several countries. Prospection of these fossil fuels demands the creation of exploratory wells. Traditionally, an exploratory well configuration is vertical, but directional or even horizontal configurations, where the boreholes are drilled following a non-vertical way, are also possible [62]. An illustration of the different types of configurations which an exploratory well can take is presented in Figure 1.

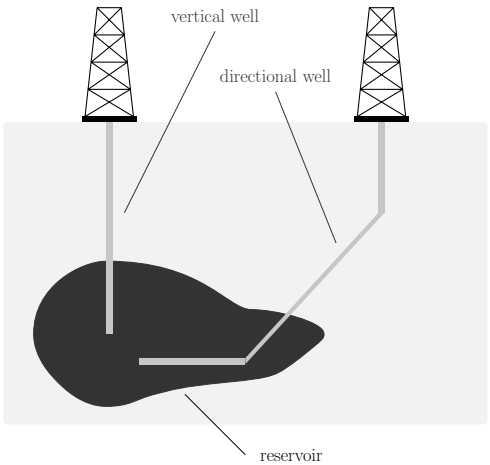

Fig. 1 Schematic representation of two exploratory wells. The left well configuration is vertical while the right one is directional.

The equipment used to drill the soil until the reservoir level is called *drillstring*. This device is a long column, composed of a sequence of connected drill-pipes and auxiliary equipment. Furthermore, within the column flows drilling mud, which is used to cool the drilling system and to remove drilling cuttings from the borehole. The bottom part of this column is called *bottom hole assembly* (BHA) and consists of a pipe of greater thickness, named *drill-colar*, and a tool used to stick the rock, the *drill-bit* [20]. The BHA presents stabilizers throughout its length, whose function is to maintain structural integrity of the borehole before cementation process. A schematic representation of a typical vertical drillstring and its components is presented in Figure 2, but a column in horizontal configuration essentially has the same structure.

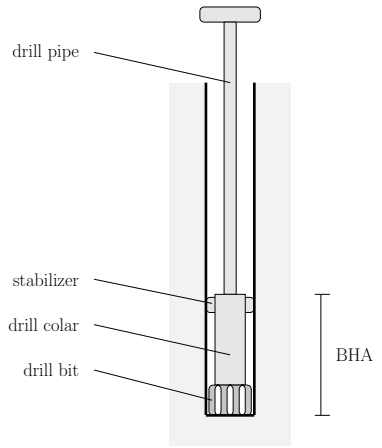

Fig. 2 Schematic representation of a typical drillstring.

Since the axial dimension of a drillstring is orders of magnitude larger than the characteristic dimension of its cross section area, the column is a long flexible structure with a very complex flexural dynamics. Furthermore, during drilling process, the drillstring is also subjected to other two mechanisms of vibration (longitudinal and torsional), which interact nonlinearly with the flexural mechanism, resulting in a further complicated dynamics [60]. The coupling between these three mechanisms of vibration, which imposes severe complications on the drillstring dynamics modeling, comes from the action of several agents, such as: structure self weight (for a vertical column); tensile and compressive loads due to the *weight on bit* (WOB) and soil reaction force; dry friction and impacts with borehole wall; bit-rock interaction forces; internal flow pressure; forces induced by internal flow instabilities; etc [60].

The dynamics of a drillstring is not a new subject in the technical/scientific literature. Works on this subject, covering experimental analysis, numerical and/or analytical modeling, can be seen since the 1960s. Most of the numerical works developed between 1960s and 1990s, have used lumped parameters approach to gain insight about drillstrings dynamical behavior. On the other hand, the analytical works focused on simple distributed parameters models. Little has been done using finite element-based approaches until the beginning of 1990s. A comprehensive literature survey of the research work produced until 2000 can be found in [10] and [60].

In recent studies, lumped parameters approach have been used, for example, to seek configurations which reduce stick-slip occurrence during drillstring operation [52]; to identify suitable values for drilling system operational parameters [32]; to analyze the coupling between axial and torsional vibrations and its stability [19, 17, 34, 15]. On the other hand, approaches based on distributed parameters models have been used to: investigate drillstring failure mechanisms [27]; better understand transversal impacts between the column and borehole wall [61]; study the effects induced by the nonlinear coupling between longitudinal and torsional dynamics of the drillstring [47]; describe the column dynamic behavior taking into account the coupling between the three mechanisms of vibration [41, 39]; investigate the chaotic regime which drillstring transverse vibration mechanism is subjected [9].

Despite the fact that directional drilling has been used in practical engineering for a few decades, and most of the exploratory wells drilled today be directional in configuration, all the works mentioned above model vertical drillstrings only. To the best of authors' knowledge, there are very few papers in open literature which models drillstring in directional configurations [46, 24, 44]. All of these works use a distributed parameters approach, but while [46, 44] only address the drillstring longitudinal dynamics, [24] uses generalized Euler-Bernoulli beam theory to describe the drillstring three-dimensional dynamics in a sloped directional well. In [46], the authors study a sloped configuration for the borehole and uses a perturbation technique to discretize the model equations. Conversely, model equations are discretized by finite element in [44].

In addition to the difficulties inherent to the nonlinear dynamics, drillstrings are subjected to randomness on their geometrical dimensions, physical properties, external forcing, etc. The lack of knowledge on these parameters, known as *system-parameter uncertainty*, is a source of inaccuracies in drillstring modeling, which may, in an extreme case, completely compromise the model predictability [49, 50]. Furthermore, during the modeling process, hypotheses about the drillstring physical behavior are made. These considerations may

be or not be in agreement with reality and should introduce additional inaccuracies in the model, known as *model uncertainty* induced by modeling errors [56, 57]. This source of uncertainty is essentially due to the use of simplified computational model for describing the phenomenon of interest and, usually, is the largest source of inaccuracy in computational model responses [56, 57].

Therefore, for a better understanding of the drillstring dynamics, these uncertainties must be modeled and quantified. In terms of quantifying these uncertainties for vertical drillstrings, the reader can see [59], where external forces are modeled as random objects and the method of statistical linearization is used along with the Monte Carlo (MC) method to treat the stochastic equations of the model. Other works in this line include: [41, 39], where system-parameter and model uncertainties are considered using a nonparametric probabilistic approach; and [43, 40], which use a standard parametric probabilistic approach to take into account the uncertainties of the system parameters. Regarding the works that model directional configurations, only [44] considers the uncertainties, which, in this case, are related to the friction effects due to drillstring/borehole wall contact.

From what is observed above, considering only the theoretical point of view, the study of drillstring nonlinear dynamics is already a rich subject. However, a good understanding of its dynamics also has significant importance in applications. For instance, it is fundamental to predict the fatigue life of the structure [33] and the drill-bit wear [68]; to analyze the structural integrity of an exploratory well [14]; to optimize the drill-bit *rate of penetration* (ROP) of into the soil [42], and the last is essential to reduce cost of production of an exploratory well.

In this sense, this study aims to analyze the three-dimensional nonlinear dynamics of a drillstring in horizontal configuration, taking into account the system-parameter uncertainties. Through this study it is expected to gain a better understanding of drillstring physics and, thus, to improve drilling process efficiency, and maximize the column ROP accordingly. All results presented here were developed in the thesis of [12].

The rest of this work is organized as follows. Section 2 presents the mechanical system of interest in this work, its parametrization and modeling from the physical point of view. Mathematical formulation of initial/boundary value problem that describes the mechanical system behavior, as well as the conservative dynamics associated, is shown in section 3. The computational modeling of the problem, which involves model equations discretization, reduction of the discretized dynamics, the algorithms for numerical integration and solution of nonlinear system of algebraic equations, can be seen in section 4. The probabilistic modeling of uncertainties is presented in section 5. Results of numerical simulations are presented and discussed in section 6. Finally, in section 7, the main conclusions are emphasized, and some paths to future works are pointed out.

2 Physical model for the problem

2.1 Definition of the mechanical system

The mechanical system of interest in this work, which is schematically represented in Figure 3, consists of a horizontal rigid pipe, perpendicular to gravity, which contains in its interior a deformable tube under rotation. This deformable tube is subjected to three-dimensional displacements, which induces longitudinal, lateral, and torsional vibrations of the structure. These mechanisms of vibration are able to generate slips and shocks in random areas of the rigid tube. Also, the contact between drill-bit, at the right extreme of the tube, with soil generates nonlinear forces and torques on drillstring right extreme, which may completely block the structure advance over the well.

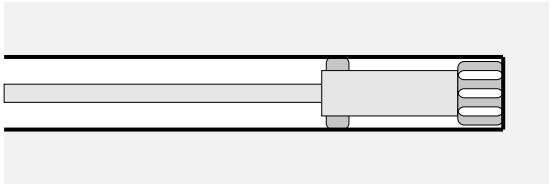

Fig. 3 Schematic representation of the mechanical system under analysis.

2.2 Nonlinear dynamical system parameterization

For purposes of modeling, the only part of column considered is the BHA. So, any variation of diameter along the column is ignored. In this way, the bottom part of the deformable tube described, in section 2.1, is modeled as a rotating beam in horizontal configuration, whose transverse displacement (y and z) at both ends is blocked, as well as transverse rotations on the left extreme. It looks like the left end of the system is a stabilizer and the right one a support. This beam is free to rotate around the x axis, and to move longitudinally. The rigid pipe is treated as a stationary cylindrical rigid wall in horizontal configuration.

As the beam is confined within the borehole, it is reasonable to assume that it undergoes small rotations

in transverse directions. On the other hand, large displacements are observed in x, y, and z, as well as large rotations around the x-axis. Therefore, the analysis that follows uses a beam theory which assumes large rotation in x, large displacements in the three spatial directions, and small deformations [5].

Seeking not to make the mathematical model excessively complex, this work will not model the fluid flow inside the beam, nor the dissipation effects induced by the flow on the system dynamics.

Due to the horizontal configuration, the beam is under action of the gravitational field, which induces an acceleration g. The beam is made of an isotropic material with mass density ρ, elastic modulus E, and Poisson's ratio ν. It has length L and annular cross section, with internal radius R_{int} and external radius R_{ext}.

An illustration of beam geometric model is presented in Figure 4. It is important to note that this model also ignores the mass of drill-bit and its geometric shape.

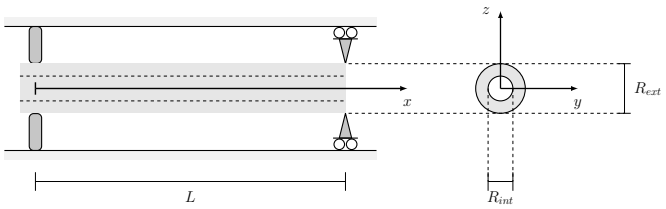

Fig. 4 Schematic representation of the beam geometry used to model the deformable tube under rotation, and the inertial system of coordinates used.

Using the cartesian coordinate system (x, y, z), defined by orthonormal basis $\{\boldsymbol{e}_x, \boldsymbol{e}_y, \boldsymbol{e}_z\}$, fixed in the inertial frame of reference $\mathcal{R}$, and shown in Figure 4, one can describe the beam undeformed configuration by

$$\mathcal{B}_b = \left\{(x, y, z) \in \mathbb{R}^3 \;\middle|\; 0 \leq x \leq L,\ (y, z) \in \mathcal{S}_b\right\}, \tag{1}$$

where the beam cross section undeformed configuration is described by

$$\mathcal{S}_b = \left\{(y, z) \in \mathbb{R}^2 \;\middle|\; R_{int}^2 \leq y^2 + z^2 \leq R_{ext}^2\right\}. \tag{2}$$

With the undeformed cross section configuration characterized, one can define and compute the cross-sectional area,

$$A = \iint_{\mathcal{S}_b} dy\, dz = \pi\left(R_{ext}^2 - R_{int}^2\right), \tag{3}$$

the second moment of area around the y axis

$$I_{yy} = \iint_{\mathcal{S}_b} z^2\, dy\, dz = I_4, \tag{4}$$

the second moment of area around the z axis

$$I_{zz} = \iint_{\mathcal{S}_b} y^2\, dy\, dz = I_4, \tag{5}$$

the polar moment of area

$$I_{xx} = \iint_{\mathcal{S}_b} \left(y^2 + z^2\right) dy\, dz = 2\, I_4, \tag{6}$$

the fourth moment of area around the z axis

$$I_{zzzz} = \iint_{\mathcal{S}_b} y^4\, dy\, dz = 3\, I_6, \tag{7}$$

and the fourth product of area

$$I_{yyzz} = \iint_{\mathcal{S}_b} y^2 z^2\, dy\, dz = I_6, \tag{8}$$

where

$$I_4 = \frac{\pi}{4}\left(R_{ext}^4 - R_{int}^4\right), \tag{9}$$

and

$$I_6 = \frac{\pi}{24}\left(R_{ext}^6 - R_{int}^6\right). \tag{10}$$

In this work other three coordinate systems (all of then with the same origin as the (x, y, z) coordinate system) are also used, each one fixed in a non-inertial frame of reference $\mathcal{R}_n$, where $n = 1, 2, 3$, and defined by an orthonormal basis of vectors of the form $\{\boldsymbol{e}_{x_n}, \boldsymbol{e}_{y_n}, \boldsymbol{e}_{z_n}\}$.

These systems of coordinates are related by a sequence of elementary rotations, such as follows

$$\underset{(x,y,z)}{\mathcal{R}} \xrightarrow{\theta_x} \underset{(x_1,y_1,z_1)}{\mathcal{R}_1} \xrightarrow{\theta_y} \underset{(x_2,y_2,z_2)}{\mathcal{R}_2} \xrightarrow{\theta_z} \underset{(x_3,y_3,z_3)}{\mathcal{R}_3}, \tag{11}$$

where θ_x is the rotation around the x axis, θ_y is the rotation around the y axis, and θ_z is the rotation around the z axis. These rotations follow the right hand rule.

Thus, with respect to the non-inertial frame of reference, the instantaneous angular velocity of rotating beam is written as

$$\boldsymbol{\omega} = \dot{\theta}_x \boldsymbol{e}_x + \dot{\theta}_y \boldsymbol{e}_{y_1} + \dot{\theta}_z \boldsymbol{e}_{z_2}, \tag{12}$$

where $\dot{\theta}_x$, $\dot{\theta}_y$, and $\dot{\theta}_z$ denote the rate of rotation around the x, y, and z directions, respectively. From now on, upper dot will be used as an abbreviation for time derivative, i.e., $\dot{\square} \equiv \frac{\partial \square}{\partial t}$.

Referencing vector $\boldsymbol{\omega}$ to the inertial frame of reference, and using the assumption of small rotations in transversal directions, one obtains

$$\boldsymbol{\omega} = \begin{pmatrix} \dot{\theta}_x + \dot{\theta}_z \theta_y \\ \dot{\theta}_y \cos\theta_x - \dot{\theta}_z \sin\theta_x \\ \dot{\theta}_y \sin\theta_x + \dot{\theta}_z \cos\theta_x \end{pmatrix}. \tag{13}$$

Regarding the kinematic hypothesis adopted for beam theory, it is assumed that the three-dimensional displacement of a beam point, occupying position (x, y, z) at instant of time t, can be written as

$$\begin{aligned} u_x(x,y,z,t) &= u - y\theta_z + z\theta_y, \\ u_y(x,y,z,t) &= v + y\,(\cos\theta_x - 1) - z\sin\theta_x, \\ u_z(x,y,z,t) &= w + z\,(\cos\theta_x - 1) + y\sin\theta_x, \end{aligned} \tag{14}$$

where u_x, u_y, and u_z respectively denote the displacement of a beam point in x, y, and z directions. Moreover, u, v, and w are the displacements of a beam neutral fiber point in x, y, and z directions, respectively.

Finally, it is possible to define the vectors

$$\boldsymbol{r} = \begin{pmatrix} x \\ y \\ z \end{pmatrix}, \quad \mathbf{v} = \begin{pmatrix} \dot{u} \\ \dot{v} \\ \dot{w} \end{pmatrix}, \quad \text{and} \quad \dot{\boldsymbol{\theta}} = \begin{pmatrix} \dot{\theta}_x \\ \dot{\theta}_y \\ \dot{\theta}_z \end{pmatrix}, \tag{15}$$

which, respectively, represent the position of a beam point, the velocity of a neutral fiber point, and the rate of rotation of a neutral fiber point.

Note that the kinematic hypothesis of Eq.(14) is expressed in terms of three spatial coordinates (x, y, and z) and six field variables (u, v, w, θ_x, θ_y, and θ_z).

It is important to mention that, as the analysis assumed small rotations in y and z, this kinematic hypothesis presents nonlinearities, expressed by trigonometric functions, only in θ_x. Besides that, since a beam theory is employed, the field variables in Eq.(14) depend only on the spatial coordinate x and time t. Therefore, although the kinematic hypothesis of Eq.(14) is three-dimensional, the mathematical model used to describe the beam nonlinear dynamics is one-dimensional.

2.3 Modeling of friction and shock effects

When a drillstring deforms laterally, there may occur a mechanical contact between the rotating beam and the borehole wall, such as illustrated in Figure 5. This mechanical contact, which generally take place via a strong impact, gives rise to friction and shock effects [21, 63, 31].

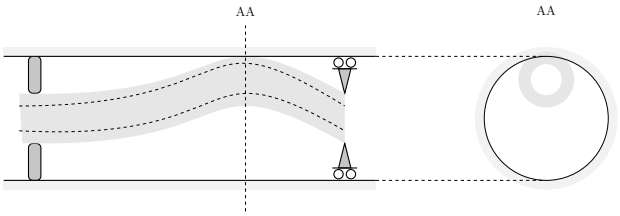

Fig. 5 Schematic representation of the situation where there is a mechanical contact between a drillstring and the borehole wall.

The modeling of friction and shock phenomena is made in terms of a geometric parameter dubbed *indentation*, which is defined as

$$\delta_{\text{FS}} = r - \texttt{gap}, \tag{16}$$

where $r = \sqrt{v^2 + w^2}$ is the neutral fiber lateral displacement, and gap denotes the spacing between the undeformed beam and the borehole wall. One has that $\delta_{\text{FS}} > 0$ in case of an impact, or $\delta_{\text{FS}} \leq 0$ otherwise, as can be seen in Figure 6. Note that the indentation corresponds to a measure of penetration in the wall of a beam cross section [21].

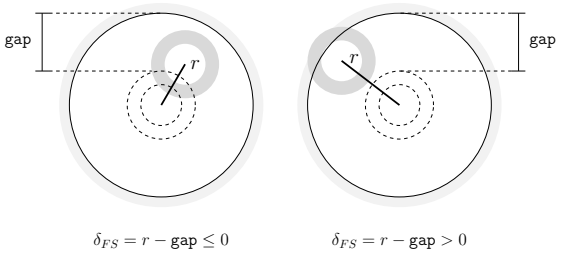

Fig. 6 Illustration of the indentation parameter in a situation without impact (left) or with impact (right).

When an impact occurs, a normal force of the form

$$F^n_{\text{FS}} = -k_{\text{FS}_1}\,\delta_{\text{FS}} - k_{\text{FS}_2}\,\delta^3_{\text{FS}} - c_{\text{FS}}\,|\delta|^3 \dot{\delta}_{\text{FS}}, \tag{17}$$

where k_{FS_1}, k_{FS_2} and c_{FS} are constants of the shock model, begins to act on the beam cross section. In this nonlinear shock model, proposed by Hunt and Crossley [26], the first (linear spring) and the second (nonlinear spring) terms describe the elastic deformation during an impact, while the third term (nonlinear damper) takes into account the loss of energy during an impact.

Once the column is rotating and moving axially, an impact also induces a frictional force in axial direction, F^a_{FS}, and a torsional friction torque, T_{FS}. Both are modeled by Coulomb friction law [11], so that the force is given by

$$F^a_{\text{FS}} = -\mu_{\text{FS}}\, F^n_{\text{FS}}\, \texttt{sgn}\,(\dot{u})\,, \tag{18}$$

where the torque is described by

$$T_{\text{FS}} = -\mu_{\text{FS}}\, F^n_{\text{FS}}\, R_{bh}\, \texttt{sgn}\left(\dot{\theta}_x\right), \tag{19}$$

being μ_{FS} the friction coefficient, $\texttt{sgn}\,(\cdot)$ the sign function, and the radius of the borehole is $R_{bh} = R_{ext} + \texttt{gap}$.

In order to find all points of contact between the beam and the borehole wall, it is necessary to discover all values of x where $\delta_{\text{FS}} > 0$. This is usually done by solving an optimization problem with constraints [65, 64].

Although the strategy of detection based on the optimization problem is robust in terms of accuracy, it is extremely complex in terms of implementation and computational cost. For this reason, this work uses an approach that introduces the forces of Eqs.(17) and (18), and the torque of Eq.(19), as efforts concentrated on the nodes of finite element mesh, defined in the section 4.1. This procedure sacrifices accuracy, but simplifies the friction and shock model implementation.

2.4 Modeling of bit-rock interaction effects

During the drilling process, in response to drillstring rotational advance, a force and a torque of reaction begin to act on the drill-bit, giving rise to the so-called bit-rock interaction effects [16, 18].

In this work, the model proposed by [44] is considered to describe the bit-rock interaction force

$$F_{\text{BR}} = \begin{cases} \Gamma_{\text{BR}}\left(e^{-\alpha_{\text{BR}}\,\dot{u}_{bit}} - 1\right) & \text{for } \dot{u}_{bit} > 0, \\ 0 & \text{for } \dot{u}_{bit} \le 0, \end{cases} \tag{20}$$

where Γ_{BR} is the bit-rock limit force, α_{BR} is the rate of change of bit-rock force, and $\dot{u}_{bit} = \dot{u}(L,\cdot)$. The graph of F_{BR} is illustrated in Figure 7.

Also, for the bit-rock interaction torque, it is adopted the regularized Coulomb model used by [28], which is expressed as

$$T_{\text{BR}} = -\mu_{\text{BR}}\, F_{\text{BR}}\, R_{bh}\, \xi_{\text{BR}}\,(\omega_{bit})\,, \tag{21}$$

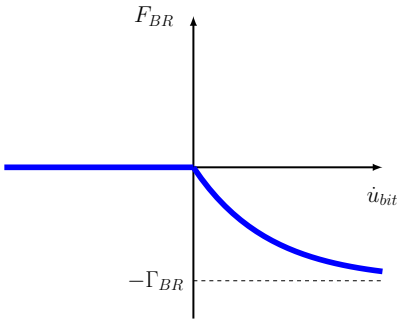

Fig. 7 Illustration of the function used to describe the reaction force on drill-bit, due to bit-rock interaction effects.

where $\omega_{bit} = \dot{\theta}_x(L,\cdot)$, the bit-rock friction coefficient is μ_{BR}, and

$$\xi_{\text{BR}}\,(\omega_{bit}) = \tanh\,(\omega_{bit}) + \frac{2\,\omega_{bit}}{1+\omega^2_{bit}}, \tag{22}$$

is a regularization function. The graph of ξ_{BR} is illustrated in Figure 8.

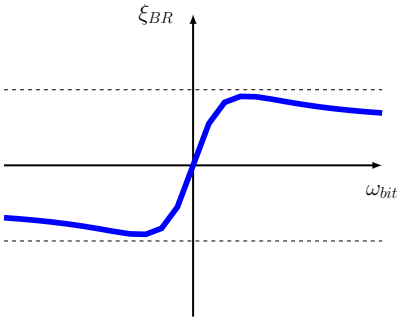

Fig. 8 Illustration of the smooth function used to regularize the reaction torque on drill-bit, due to bit-rock interaction effects.

2.5 Kinetic energy

The kinetic energy of rotating beam is given by

$$\mathcal{T} = \frac{1}{2}\iiint_{\mathcal{B}_b} \rho\, \mathbf{v}\cdot\mathbf{v}\, dx\, dy\, dz \;+ \\ \frac{1}{2}\iiint_{\mathcal{B}_b} \rho\, \boldsymbol{\omega}\cdot\left(\boldsymbol{r}\cdot\boldsymbol{r}\,\mathbb{I} - \boldsymbol{r}\otimes\boldsymbol{r}\right)\boldsymbol{\omega}\, dx\, dy\, dz, \tag{23}$$

where first triple integral corresponds to beam translational kinetic energy, and the second one is associated to beam rotational kinetic energy. In this equation, $\mathbb{I}$ denotes the identity tensor, the symbol $\cdot$ represents the standard inner product between two Euclidean vectors,

and the symbol $\otimes$ is used to designate the tensor product.

Developing the vector operations indicated in Eq.(23), using (1) and (2) to define the limits of integration, using the definitions of A, I_{yy}, I_{zz}, and I_{xx}, and making the other calculations one can show that Eq.(23) is equivalent to

$$\begin{aligned}\mathcal{T} = &\frac{1}{2}\int_{x=0}^{L} \rho\, A \left(\dot{u}^2 + \dot{v}^2 + \dot{w}^2\right) dx \;+ \\ &\frac{1}{2}\int_{x=0}^{L} 2\,\rho\, I_4 \left(\dot{\theta}_x + \dot{\theta}_z\theta_y\right)^2 dx \;+ \\ &\frac{1}{2}\int_{x=0}^{L} \rho\, I_4 \left(\dot{\theta}_y \cos\theta_x - \dot{\theta}_z \sin\theta_x\right)^2 dx \;+ \\ &\frac{1}{2}\int_{x=0}^{L} \rho\, I_4 \left(\dot{\theta}_y \sin\theta_x + \dot{\theta}_z \cos\theta_x\right)^2 dx.\end{aligned} \tag{24}$$

2.6 Strain energy

The analysis of the beam assumes that it is subjected to large displacements, and small deformations. In this way, its strain energy is given by

$$\mathcal{V} = \frac{1}{2}\iiint_{\mathcal{B}_b} \boldsymbol{\epsilon} : \boldsymbol{\sigma}\, dx\, dy\, dz, \tag{25}$$

where $\boldsymbol{\epsilon}$ denotes the Green-Lagrangian strain tensor, $\boldsymbol{\sigma}$ is the second Piola-Kirchhoff stress tensor, and the symbol $:$ represents the double inner product between two tensors.

It is further considered that the beam is made of an isotropic material, such that stress and strain are related by the following constitutive equation (Hooke's law)

$$\boldsymbol{\sigma} = 2\,G\,\boldsymbol{\epsilon} + \lambda\,\mathtt{tr}\,(\boldsymbol{\epsilon})\,\mathbb{I}, \tag{26}$$

where $\mathtt{tr}\,(\cdot)$ represents the trace operator, G is material shear modulus, and λ is used to designate the material first Lamé parameter. In terms of the elastic modulus E and the Poisson's ratio ν, these elastic parameters can be written as

$$G = \frac{E}{2\,(1+\nu)}, \qquad \text{and} \qquad \lambda = \frac{E\,\nu}{(1+\nu)(1-2\,\nu)}. \tag{27}$$

According to the beam theory used in this work, there is no tension in any cross section of the beam that is perpendicular to x axis, i.e., $\sigma_{yy} = 0$, $\sigma_{zz} = 0$, $\sigma_{yz} = 0$, and $\sigma_{zy} = 0$. When this hypothesis is combined with the three-dimensional Hooke's law, represented by Eq.(26), one can conclude that $\sigma_{xx} = E\,\epsilon_{xx}$, $\sigma_{xy} = 2\,G\,\epsilon_{xy}$, and $\sigma_{xz} = 2\,G\,\epsilon_{xz}$, which is an one-dimensional version of Hooke's law.

Combining this one-dimensional Hooke's law with the stress tensor symmetry, one can express the double contraction between strain and stress tensors, within the integral in Eq.(25), as a quadratic form

$$\boldsymbol{\epsilon} : \boldsymbol{\sigma} = E\,\epsilon_{xx}^2 + 4\,G\,\epsilon_{xy}^2 + 4\,G\,\epsilon_{xz}^2, \tag{28}$$

which is modified, by the introduction of shearing factor κ_s, as

$$\boldsymbol{\epsilon} : \boldsymbol{\sigma} = E\,\epsilon_{xx}^2 + 4\,\kappa_s\,G\,\epsilon_{xy}^2 + 4\,\kappa_s\,G\,\epsilon_{xz}^2. \tag{29}$$

This modification aims to take into account the effect of shear deformation in the beam cross section area, which is neglected when one uses the one-dimensional Hooke's law.

Hence, after replace Eq.(29) in Eq.(25), one finally obtains

$$\mathcal{V} = \frac{1}{2}\iiint_{\mathcal{B}_b} \left(E\,\epsilon_{xx}^2 + 4\,\kappa_s\,G\,\epsilon_{xy}^2 + 4\,\kappa_s\,G\,\epsilon_{xz}^2\right) dx\, dy\, dz. \tag{30}$$

As the analysis is using large displacements, one has

$$\begin{aligned}\epsilon_{xx} = &\frac{1}{2}\left(\frac{\partial u_x}{\partial x} + \frac{\partial u_x}{\partial x}\right) \;+ \\ &\frac{1}{2}\left(\frac{\partial u_x}{\partial x}\frac{\partial u_x}{\partial x} + \frac{\partial u_y}{\partial x}\frac{\partial u_y}{\partial x} + \frac{\partial u_z}{\partial x}\frac{\partial u_z}{\partial x}\right),\end{aligned} \tag{31}$$

$$\begin{aligned}\epsilon_{xy} = &\frac{1}{2}\left(\frac{\partial u_y}{\partial x} + \frac{\partial u_x}{\partial y}\right) \;+ \\ &\frac{1}{2}\left(\frac{\partial u_x}{\partial x}\frac{\partial u_x}{\partial y} + \frac{\partial u_y}{\partial x}\frac{\partial u_y}{\partial y} + \frac{\partial u_z}{\partial x}\frac{\partial u_z}{\partial y}\right),\end{aligned} \tag{32}$$

and

$$\begin{aligned}\epsilon_{xz} = &\frac{1}{2}\left(\frac{\partial u_z}{\partial x} + \frac{\partial u_x}{\partial z}\right) \;+ \\ &\frac{1}{2}\left(\frac{\partial u_x}{\partial x}\frac{\partial u_x}{\partial z} + \frac{\partial u_y}{\partial x}\frac{\partial u_y}{\partial z} + \frac{\partial u_z}{\partial x}\frac{\partial u_z}{\partial z}\right),\end{aligned} \tag{33}$$

where the quadratic terms on the right hand side of the above equations are associated to beam model geometric nonlinearity.

Substituting the kinematic hypothesis of Eq.(14) in Eqs.(31) to (33), and then calculating the partial derivatives, one concludes that the deformations are respectively given by

$$\begin{aligned}\epsilon_{xx} = \quad & u' - y\,\theta_z' + z\,\theta_y' + u'\left(z\,\theta_y' - y\,\theta_z'\right) - y\,z\,\theta_y'\,\theta_z' + \\ & \theta_x'\left(\left(y\,w' - z\,v'\right)\cos\theta_x - \left(y\,v' + z\,w'\right)\sin\theta_x\right) + \\ & \frac{1}{2}\left(u'^2 + v'^2 + w'^2 + y^2\,\theta_z'^2 + z^2\,\theta_y'^2 + \left(y^2+z^2\right)\theta_x'^2\right),\end{aligned} \tag{34}$$

$$\begin{aligned}\epsilon_{xy} = & \frac{1}{2}\left(v'\,\cos\theta_x + w'\sin\theta_x - z\,\theta_x'\right) + \\ & \frac{1}{2}\,\theta_z\left(y\,\theta_z' - z\theta_y' - u' - 1\right),\end{aligned} \tag{35}$$

and

$$\begin{aligned}\epsilon_{xz} = & \frac{1}{2}\left(w'\,\cos\theta_x - v'\sin\theta_x + y\,\theta_x'\right) + \\ & \frac{1}{2}\,\theta_y\left(-y\,\theta_z' + z\theta_y' + u' + 1\right),\end{aligned} \tag{36}$$

where prime is used as an abbreviation for space derivative, i.e., $\square' \equiv \frac{\partial \square}{\partial x}$.

2.7 Energy dissipation function

It is assumed that the beam loses energy through a mechanism of viscous dissipation, with a (dimensionless) damping constant c. In this way, there is an energy dissipation function (per unit of length) associated to the system, which is given by

$$\begin{aligned}\mathcal{D} = & \frac{1}{2}\iint_{\mathcal{S}_b} c\,\rho\,\mathbf{v}\cdot\mathbf{v}\,dy\,dz + \\ & \frac{1}{2}\iint_{\mathcal{S}_b} c\,\rho\,\dot{\boldsymbol{\theta}}\cdot\left(\boldsymbol{r}\cdot\boldsymbol{r}\,\mathbb{I} - \boldsymbol{r}\otimes\boldsymbol{r}\right)\dot{\boldsymbol{\theta}}\,dy\,dz,\end{aligned} \tag{37}$$

where the first term is a dissipation potential due to the translational movement, and the second term represents a dissipation potential due to the movement of rotation.

Making a development almost similar to the one performed to obtain Eq.(24), it can be shown that

$$\begin{aligned}\mathcal{D} = & \frac{1}{2}\,c\,\rho\,A\left(\dot{u}^2 + \dot{v}^2 + \dot{w}^2\right) + \\ & \frac{1}{2}\,c\,\rho\,I_4\left(2\,\dot{\theta}_x^2 + \dot{\theta}_y^2 + \dot{\theta}_z^2\right).\end{aligned} \tag{38}$$

2.8 External forces work

The work done by the external forces acting on the beam is given by

$$\mathcal{W} = -\int_{x=0}^{L} \rho\,A\,g\,w\,dx + \mathcal{W}_{\text{FS}} + \mathcal{W}_{\text{BR}}, \tag{39}$$

where the first term is due to gravity, the second one is associated to friction and shock effects, and the last term accounts the work done by the force/torque that comes from bit-rock interaction.

Note that, due to non-holonomic nature of the forces and torques that comes from the effects of friction/shock, and bit-rock interaction, it is not possible to write explicit formulas for $\mathcal{W}_{\text{FS}}$ and $\mathcal{W}_{\text{FS}}$ [30].

However, it is known that the virtual work of $\mathcal{W}_{\text{FS}}$, denoted by $\delta\mathcal{W}_{\text{FS}}$, is written as

$$\delta\mathcal{W}_{\text{FS}} = \sum_{m=1}^{N_{nodes}} \left(F_{\text{FS}}^{a}\,\delta u + F_{\text{FS}}^{n}\left(v\,\delta v + w\,\delta w\right)/r + T_{\text{FS}}\,\delta\theta_x\right)\Big|_{x=x_m} \tag{40}$$

where x_m are the global coordinates of finite element nodes, N_{nodes} is the number of nodes in finite element mesh, and δu, δv, δw, and $\delta\theta_x$ respectively denote the variations of u, v, w, and θ_x.

On the other hand, the virtual work of $\mathcal{W}_{\text{BR}}$, denoted by $\delta\mathcal{W}_{\text{BR}}$, reads as

$$\delta\mathcal{W}_{\text{BR}} = F_{\text{BR}}\,\delta u\Big|_{x=L} + T_{\text{BR}}\,\delta\theta_x\Big|_{x=L}. \tag{41}$$

3 Mathematical model for the problem

3.1 Equation of motion of the nonlinear dynamics

A modified version of Hamilton's extended principle [30] is employed to derive the equations which describe the mechanical system nonlinear dynamics, so that the first variation is expressed as

$$\int_{t=t_0}^{t_f}\left(\delta\mathcal{T} - \delta\mathcal{V} + \delta\mathcal{W}\right)dt - \int_{t=t_0}^{t_f}\int_{x=0}^{L}\delta\boldsymbol{U}\cdot\frac{\partial\mathcal{D}}{\partial\dot{\boldsymbol{U}}}\,dx\,dt = 0, \tag{42}$$

where the first term corresponds to dynamics conservative part, and the second one is associated to energy dissipation. Also, $\boldsymbol{U}$ is a vector field which lumps the field variables, the initial and final instants of observation are respectively denoted by t_0 and t_f, and the symbol δ represents the variation operator [45].

The development of Eq.(42) results in the following weak equation of motion

$$\mathcal{M}\left(\boldsymbol{\psi},\ddot{\boldsymbol{U}}\right) + \mathcal{C}\left(\boldsymbol{\psi},\dot{\boldsymbol{U}}\right) + \mathcal{K}\left(\boldsymbol{\psi},\boldsymbol{U}\right) = \mathcal{F}\left(\boldsymbol{\psi},\boldsymbol{U},\dot{\boldsymbol{U}},\ddot{\boldsymbol{U}}\right), \tag{43}$$

valid for any $\boldsymbol{\psi}$ chosen in a "suitable" space of weight functions, where the field variables and their corresponding weight functions are represented by the vector fields $\boldsymbol{U} = \left(u, v, w, \theta_x, \theta_y, \theta_z\right)$, and $\boldsymbol{\psi} = \left(\psi_u, \psi_v, \psi_w, \psi_{\theta_x}, \psi_{\theta_y}, \psi_{\theta_z}\right)$.

Furthermore,

$$\mathcal{M}\left(\boldsymbol{\psi},\ddot{\boldsymbol{U}}\right) = \int_{x=0}^{L} \rho\, A\left(\psi_u\,\ddot{u} + \psi_v\,\ddot{v} + \psi_w\,\ddot{w}\right) dx \;+ \int_{x=0}^{L} \rho\, I_4\left(2\,\psi_{\theta_x}\,\ddot{\theta}_x + \psi_{\theta_y}\,\ddot{\theta}_y + \psi_{\theta_z}\,\ddot{\theta}_z\right) dx, \tag{44}$$

represents the mass operator,

$$\mathcal{C}\left(\boldsymbol{\psi},\dot{\boldsymbol{U}}\right) = \int_{x=0}^{L} c\,\rho\, A\left(\psi_u\,\dot{u} + \psi_v\,\dot{v} + \psi_w\,\dot{w}\right) dx \;+ \int_{x=0}^{L} c\,\rho\, I_4\left(2\,\psi_{\theta_x}\,\dot{\theta}_x + \psi_{\theta_y}\,\dot{\theta}_y + \psi_{\theta_z}\,\dot{\theta}_z\right) dx, \tag{45}$$

is the damping operator,

$$\begin{aligned}\mathcal{K}\left(\boldsymbol{\psi},\boldsymbol{U}\right) = &\int_{x=0}^{L} E\,A\,\psi_u'\,u'\,dx \;+ \\ &\int_{x=0}^{L} E\,I_4\left(\psi_{\theta_y}'\,\theta_y' + \psi_{\theta_z}'\,\theta_z'\right) dx \;+ \\ &\int_{x=0}^{L} 2\,\kappa_s\,G\,I_4\,\psi_{\theta_x}'\,\theta_x'\,dx \;+ \\ &\int_{x=0}^{L} \kappa_s\,G\,A\left(\psi_{\theta_y} + \psi_w'\right)\left(\theta_y + w'\right) dx \;+ \\ &\int_{x=0}^{L} \kappa_s\,G\,A\left(\psi_{\theta_z} - \psi_v'\right)\left(\theta_z - v'\right) dx,\end{aligned} \tag{46}$$

is the stiffness operator, and

$$\begin{aligned}\mathcal{F}\left(\boldsymbol{\psi},\boldsymbol{U},\dot{\boldsymbol{U}},\ddot{\boldsymbol{U}}\right) = &\mathcal{F}_{\text{KE}}\left(\boldsymbol{\psi},\boldsymbol{U},\dot{\boldsymbol{U}},\ddot{\boldsymbol{U}}\right) + \\ &\mathcal{F}_{\text{SE}}\left(\boldsymbol{\psi},\boldsymbol{U}\right) \;+\; \mathcal{F}_{\text{FS}}\left(\boldsymbol{\psi},\boldsymbol{U}\right) \;+ \\ &\mathcal{F}_{\text{BR}}\left(\boldsymbol{\psi},\dot{\boldsymbol{U}}\right) \;+\; \mathcal{F}_{\text{G}}\left(\boldsymbol{\psi}\right),\end{aligned} \tag{47}$$

is the force operator, which is divided into five parts. A nonlinear force due to inertial effects

$$\begin{aligned}\mathcal{F}_{\text{KE}} = &-\int_{x=0}^{L} 2\,\rho\, I_4\,\psi_{\theta_x}\left(\theta_y\,\ddot{\theta}_z + \dot{\theta}_y\,\dot{\theta}_z\right) dx \\ &+\int_{x=0}^{L} 2\,\rho\, I_4\,\psi_{\theta_y}\left(\theta_y\,\dot{\theta}_z^2 + \dot{\theta}_x\,\dot{\theta}_z\right) dx \\ &-\int_{x=0}^{L} 2\,\rho\, I_4\,\psi_{\theta_z}\left(\theta_y\,\ddot{\theta}_x + \theta_y^2\,\ddot{\theta}_z\right) dx \\ &-\int_{x=0}^{L} 2\,\rho\, I_4\,\psi_{\theta_z}\left(\dot{\theta}_x\,\dot{\theta}_y + 2\,\theta_y\,\dot{\theta}_y\,\dot{\theta}_z\right) dx,\end{aligned} \tag{48}$$

a nonlinear force due to geometric nonlinearity

$$\begin{aligned}\mathcal{F}_{\text{SE}} = &\int_{x=0}^{L}\left(\psi_{\theta_x}\,\Gamma_1 + \psi_{\theta_y}\,\Gamma_2 + \psi_{\theta_z}\,\Gamma_3\right) dx \;+ \\ &\int_{x=0}^{L}\left(\psi_u'\,\Gamma_4 + \psi_v'\,\Gamma_5 + \psi_w'\,\Gamma_6\right) dx \;+ \\ &\int_{x=0}^{L}\left(\psi_{\theta_x}'\,\Gamma_7 + \psi_{\theta_y}'\,\Gamma_8 + \psi_{\theta_z}'\,\Gamma_9\right) dx,\end{aligned} \tag{49}$$

a nonlinear force due to friction and shock effects

$$\mathcal{F}_{\text{FS}} = \sum_{m=1}^{N_{nodes}}\left(F_{\text{FS}}^{a}\,\psi_u + F_{\text{FS}}^{n}\left(v\,\psi_v + w\,\psi_w\right)/r + T_{\text{FS}}\,\psi_{\theta_x}\right)\Big|_{x=x_m} \tag{50}$$

a nonlinear force due to bit-rock interaction

$$\mathcal{F}_{\text{BR}} = F_{\text{BR}}\,\psi_u\Big|_{x=L} + T_{\text{BR}}\,\psi_{\theta_x}\Big|_{x=L}, \tag{51}$$

and a linear force due to gravity

$$\mathcal{F}_{\text{G}} = -\int_{x=0}^{L} \rho\, A\, g\,\psi_w\, dx. \tag{52}$$

The nonlinear functions Γ_n, with $n = 1, \cdots, 9$, in Eq.(49) are very complex and, for sake of space limitation, are not presented in this section. But they can be seen in Appendix A.

The model presented above is an adaptation, for horizontal drillstrings, of the model proposed by [41, 39] to describe the nonlinear dynamics of vertical drillstrings. To be more precise, in the reference problem gravity is parallel to drillstring main axis, while in this work, it is perpendicular to the structure primal direction. Therefore, the former problem primarily addresses the dynamics of a column, while the new problem deals with the dynamics of a beam. Also, the original problem treated the nonlinear dynamics around a pre-stressed equilibrium configuration, while the new problem does not consider the dynamics around any particular configuration. It is worth mentioning that changes made in the modeling of friction and shock effects are significant. For instance, a nonlinear shock model that also takes into account the dissipation of energy during an impact is introduced, in contrast to the reference work, that only consider the linear elastic deformation effects. In addition, the boundary conditions are different, as well as the bit-rock interaction model. On the other hand, for the sake of simplicity, the fluid structure interaction effects, considered in reference work are neglected in this study.

3.2 Initial conditions

With regard to mechanical system initial state, it is assumed that the beam presents neither displacement nor rotations, i.e., $u(x,0)=0$, $v(x,0)=0$, $w(x,0)=0$, $\theta_x(x,0)=0$, $\theta_y(x,0)=0$, and $\theta_z(x,0)=0$. These field variables, except for u and θ_x, also have initial velocities and rate of rotations equal to zero, i.e. $\dot{v}(x,0)=0$, $\dot{w}(x,0)=0$, $\dot{\theta}_y(x,0)=0$, and $\dot{\theta}_z(x,0)=0$.

It is also assumed that, initially, the beam moves horizontally with a constant axial velocity V_0, and rotates around the x axis with a constant angular velocity Ω. Thereby, one has that $\dot{u}(x,0)=V_0$, and $\dot{\theta}_x(x,0)=\Omega$.

Projecting the initial conditions in a "suitable" space of weight functions, weak forms for them are obtained, respectively, given by

$$\mathcal{M}\left(\boldsymbol{\psi},\boldsymbol{U}(0)\right)=\mathcal{M}\left(\boldsymbol{\psi},\boldsymbol{U}_0\right), \tag{53}$$

and

$$\mathcal{M}\left(\boldsymbol{\psi},\dot{\boldsymbol{U}}(0)\right)=\mathcal{M}\left(\boldsymbol{\psi},\dot{\boldsymbol{U}}_0\right), \tag{54}$$

where $\boldsymbol{U}_0=(0,0,0,0,0,0)$ and $\dot{\boldsymbol{U}}_0=(V_0,0,0,\Omega,0,0)$.

In formal terms, the weak formulation of the initial–boundary value problem that describes the mechanical system nonlinear dynamics consists in find a vector field $\boldsymbol{U}$, "sufficiently regular", which satisfies the weak equation of motion given by Eq.(43) for all "suitable" $\boldsymbol{\psi}$, as well as the weak form of initial conditions, given by Eqs.(53), and (54) [25].

3.3 Associated linear conservative dynamics

Consider the linear homogeneous equation given by

$$\mathcal{M}\left(\boldsymbol{\psi},\ddot{\boldsymbol{U}}\right)+\mathcal{K}\left(\boldsymbol{\psi},\boldsymbol{U}\right)=0, \tag{55}$$

obtained from Eq.(43) when one discards the damping, and force operators, and which is valid for all $\boldsymbol{\psi}$ in the space of weight functions.

Suppose that Eq.(55) has a solution of the form $\boldsymbol{U}=e^{i\omega t}\boldsymbol{\phi}$, where ω is a natural frequency (in rad/s), $\boldsymbol{\phi}$ is the associated normal mode, and $i=\sqrt{-1}$ is the imaginary unit. Replacing this expression of $\boldsymbol{U}$ in Eq.(55) and using the linearity of operators $\mathcal{M}$, and $\mathcal{K}$, one gets

$$\left(-\omega^2\mathcal{M}\left(\boldsymbol{\psi},\boldsymbol{\phi}\right)+\mathcal{K}\left(\boldsymbol{\psi},\boldsymbol{\phi}\right)\right)e^{i\omega t}=0, \tag{56}$$

which is equivalent to

$$-\omega^2\mathcal{M}\left(\boldsymbol{\psi},\boldsymbol{\phi}\right)+\mathcal{K}\left(\boldsymbol{\psi},\boldsymbol{\phi}\right)=0, \tag{57}$$

a generalized eigenvalue problem.

Since operator $\mathcal{M}$ is positive-definite, and operator $\mathcal{K}$ is positive semi-definite, the generalized eigenvalue problem above has a denumerable number of solutions. The solutions of this eigenvalue problem have the form $(\omega_n^2,\boldsymbol{\phi}_n)$, where ω_n is the n-th natural frequency and $\boldsymbol{\phi}_n$ is the n-th normal mode [23].

Also, the symmetry of operators $\mathcal{M}$, and $\mathcal{K}$ implies the following orthogonality relations

$$\mathcal{M}\left(\boldsymbol{\phi}_n,\boldsymbol{\phi}_m\right)=\delta_{nm},\quad\text{and}\quad\mathcal{K}\left(\boldsymbol{\phi}_n,\boldsymbol{\phi}_m\right)=\omega_n^2\,\delta_{nm}, \tag{58}$$

where δ_{nm} represents the Kronecker delta symbol. See [23] for more details.

The generalized eigenvalue problem of Eq.(57), as well as the properties of (58), will be useful to construct a reduced order model for discretized dynamical system which approximates the solution of the weak initial–boundary value problem of Eqs.(43), (53), and (54).

4 Computational model for the problem

4.1 Discretization of the nonlinear dynamics

To proceed with the discretization of the weak initial–boundary value problem of Eqs.(43), (53), and (54), which describes the rotating beam nonlinear dynamics, it is used the standard finite element method (FEM) [25], where the spaces of basis and weight functions are constructed by the same (finite dimensional) class of functions.

In this procedure, the beam geometry is discretized by a FEM mesh with N_{elem} finite elements. Each one of these elements is composed by two nodes, and each one of these nodes has six degrees of freedom associated, one for each field variable in the beam model described in section 3.1. Thus, the number of degrees of freedom associated with FEM model is $N_{dofs}=6(N_{elem}+1)$. An illustration of FEM mesh/element can be seen in Figure 9.

Concerning the shape functions, it is adopted an interdependent interpolation scheme which avoids shear-locking effect [38]. This scheme uses, for transverse displacements/rotations, Hermite cubic polynomials, and, for the fields of axial displacement/torsional rotation, affine functions [2].

Thus, each field variable of the physical model is approximated by a linear combination of basis functions, in such way that

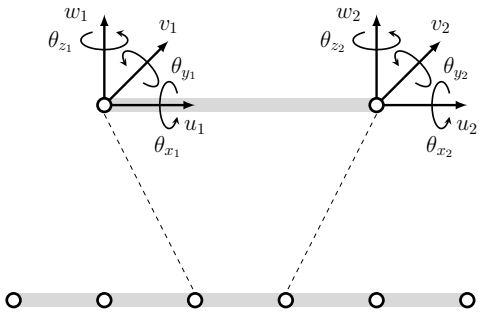

Fig. 9 Illustration of FEM mesh/element used to discretize the beam geometry.

$$
\begin{aligned}
u(x,t) &\approx \sum_{m=1}^{N_{dofs}} Q_m(t)\,\mathcal{N}_m(x), \qquad (59)\\
\theta_x(x,t) &\approx \sum_{m=1}^{N_{dofs}} Q_m(t)\,\mathcal{N}_m(x),\\
v(x,t) &\approx \sum_{m=1}^{N_{dofs}} Q_m(t)\,\mathcal{H}_m^{(1)}(x),\\
w(x,t) &\approx \sum_{m=1}^{N_{dofs}} Q_m(t)\,\mathcal{H}_m^{(1)}(x),\\
\theta_y(x,t) &\approx \sum_{m=1}^{N_{dofs}} Q_m(t)\,\mathcal{H}_m^{(2)}(x),\\
\theta_z(x,t) &\approx \sum_{m=1}^{N_{dofs}} Q_m(t)\,\mathcal{H}_m^{(2)}(x),
\end{aligned}
$$

where $\mathcal{N}_m(x)$, $\mathcal{H}_m^{(1)}(x)$, and $\mathcal{H}_m^{(2)}(x)$ are the (position dependent) shape functions, and $Q_m(t)$ are the (time dependent) coefficients of the linear combination. In physical terms, each one of these temporal coefficients represents a degree of freedom of the FEM model.

The discretization results is the $N_{dofs} \times N_{dofs}$ nonlinear system of ordinary differential equations given by

$$
[\mathcal{M}]\,\ddot{\boldsymbol{Q}}(t) + [\mathcal{C}]\,\dot{\boldsymbol{Q}}(t) + [\mathcal{K}]\,\boldsymbol{Q}(t) = \boldsymbol{\mathcal{F}}\left(\boldsymbol{Q}, \dot{\boldsymbol{Q}}, \ddot{\boldsymbol{Q}}\right), \qquad (60)
$$

where $\boldsymbol{Q}(t)$ is the nodal displacement vector (translations and rotations), $\dot{\boldsymbol{Q}}(t)$ is the nodal velocity vector, and $\ddot{\boldsymbol{Q}}(t)$ is the nodal acceleration vector. The other objects in Eq.(60) are the mass matrix $[\mathcal{M}]$, the damping matrix $[\mathcal{C}]$, the stiffness matrix $[\mathcal{K}]$, and the force vector $\boldsymbol{\mathcal{F}}$.

A discretization procedure similar to one presented above is applied to the initial conditions of Eqs.(53) and (54), which results in linear systems of algebraic equations given by

$$
[\mathcal{M}]\,\boldsymbol{Q}(0) = \boldsymbol{Q}_0, \qquad \text{and} \qquad [\mathcal{M}]\,\dot{\boldsymbol{Q}}(0) = \dot{\boldsymbol{Q}}_0. \qquad (61)
$$

4.2 Reduction of finite element model

In order to reduce the dimension of finite element model developed in section 4.1, it is considered a finite dimensional version of the generalized eigenvalue problem presented in section 3.3, which is defined by

$$
[\mathcal{K}]\,\boldsymbol{\phi}_n = \omega_n^2\,[\mathcal{M}]\,\boldsymbol{\phi}_n. \qquad (62)
$$

Due to the properties of $\mathcal{M}$, and $\mathcal{K}$ operators, discussed in section 3.3, and inherited by finite dimensional operators $[\mathcal{M}]$ and $[\mathcal{K}]$, the above eigenvalue problem has N_{dofs} solutions. But Eq.(62) is solved only for $n = 1, 2, \cdots, N_{red}$, where the reduced model dimension N_{red} is an integer chosen such that $N_{red} \ll N_{dofs}$.

The procedure that follows consists in project the nonlinear dynamics, defined by the initial value problem of Eqs.(60) and (61), into the vector space spanned by $\{\boldsymbol{\phi}_1, \boldsymbol{\phi}_2, \cdots, \boldsymbol{\phi}_{N_{red}}\}$.

For this purpose, define the $N_{dofs} \times N_{red}$ projection matrix by

$$
[\Phi] = \begin{bmatrix} | & | & & | \\ \boldsymbol{\phi}_1 & \boldsymbol{\phi}_2 & \cdots & \boldsymbol{\phi}_{N_{red}} \\ | & | & & | \end{bmatrix}, \qquad (63)
$$

make in Eqs.(60) and (61) the change of basis defined by

$$
\boldsymbol{Q}(t) = [\Phi]\,\boldsymbol{q}(t), \qquad (64)
$$

and then pre-multiply the resulting equations by matrix $[\Phi]^T$, where superscript ^{T} represents the transposition operation.

This development results in the reduced initial value problem given by

$$
[M]\,\ddot{\boldsymbol{q}}(t) + [C]\,\dot{\boldsymbol{q}}(t) + [K]\,\boldsymbol{q}(t) = \boldsymbol{f}\left(\boldsymbol{q}(t), \dot{\boldsymbol{q}}(t), \ddot{\boldsymbol{q}}(t)\right), \qquad (65)
$$

and

$$
\boldsymbol{q}(0) = \boldsymbol{q}_0, \qquad \text{and} \qquad \dot{\boldsymbol{q}}(0) = \dot{\boldsymbol{q}}_0, \qquad (66)
$$

where $\boldsymbol{q}(t)$ is the reduced displacement vector, $\dot{\boldsymbol{q}}(t)$ is the reduced velocity vector, $\ddot{\boldsymbol{q}}(t)$ is the reduced acceleration vector. The reduced matrices of mass, damping,

and stiffness, as well as the reduced vectors of force, initial displacement, and initial velocity are, respectively, defined by $[M] = [\Phi]^T [\mathcal{M}] [\Phi]$, $[C] = [\Phi]^T [\mathcal{C}] [\Phi]$, $[K] = [\Phi]^T [\mathcal{K}] [\Phi]$, $\boldsymbol{f} = [\Phi]^T \boldsymbol{\mathcal{F}} \left([\Phi]\, \boldsymbol{q}(t), [\Phi]\, \dot{\boldsymbol{q}}(t), [\Phi]\, \ddot{\boldsymbol{q}}(t)\right)$, $\boldsymbol{q}_0 = [\Phi]^T \boldsymbol{Q}_0$, $\dot{\boldsymbol{q}}_0 = [\Phi]^T \dot{\boldsymbol{Q}}_0$. These matrices are $N_{red} \times N_{red}$, while these vectors are $N_{red} \times 1$. Furthermore, due to the orthogonality properties defined by Eq.(58), that are inherited by the operators in finite dimension, these matrices are diagonal.

Thus, although the initial value problem of Eqs.(65) and (66) is apparently similar to the one defined by Eqs.(60) and (61), the former has a structure that makes it much more efficient in terms of computational cost, and so, it will be used to analyze the nonlinear dynamics under study.

4.3 Integration of discretized nonlinear dynamics

In order to solve the initial value problem of Eqs.(65) and (66), it is employed the Newmark method [35], which defines the following implicit integration scheme

$$\dot{\boldsymbol{q}}_{n+1} = \dot{\boldsymbol{q}}_n + (1-\gamma)\Delta t\, \ddot{\boldsymbol{q}}_n + \gamma \Delta t\, \ddot{\boldsymbol{q}}_{n+1}, \tag{67}$$

$$\boldsymbol{q}_{n+1} = \boldsymbol{q}_n + \Delta t\, \dot{\boldsymbol{q}}_n + \left(\frac{1}{2} - \beta\right) \Delta t^2\, \ddot{\boldsymbol{q}}_n + \beta\, \Delta t^2\, \ddot{\boldsymbol{q}}_{n+1}, \tag{68}$$

where $\boldsymbol{q}_n$, $\dot{\boldsymbol{q}}_n$ and $\ddot{\boldsymbol{q}}_n$ are approximations to $\boldsymbol{q}(t_n)$, $\dot{\boldsymbol{q}}(t_n)$ and $\ddot{\boldsymbol{q}}(t_n)$, respectively, and $t_n = n\Delta t$ is an instant in a temporal mesh defined over the interval $[t_0, t_f]$, with an uniform time step Δt. The parameters γ and β are associated with accuracy and stability of the numerical scheme [25], and for the simulations reported in this work they are assumed as $\gamma = 1/2 + \alpha$, and $\beta = 1/4\left(1/2 + \gamma\right)^2$, with $\alpha = 15/1000$.

Handling up properly Eqs.(67) and (68), and the discrete version of Eq.(65), one arrives in a nonlinear system of algebraic equations, with unknown vector $\boldsymbol{q}_{n+1}$, which is represented by

$$[\hat{K}]\boldsymbol{q}_{n+1} = \hat{\boldsymbol{f}}_{n+1}\left(\boldsymbol{q}_{n+1}\right), \tag{69}$$

where $[\hat{K}]$ is the effective stiffness matrix, and $\hat{\boldsymbol{f}}_{n+1}$ is the (nonlinear) effective force vector.

4.4 Incorporation of boundary conditions

As can be seen in Figure 4, the mechanical system has the following boundary conditions: (i) left extreme with no transversal displacement, nor transversal rotation; (ii) right extreme with no transversal displacement. It is also assumed that the left end has: (iii) constant axial and rotational velocities in x, respectively equal to V_0 and Ω.

Hence, for $x = 0$, it is true that $u(0,t) = V_0\, t$, $v(0,t) = 0$, $w(0,t) = 0$, $\theta_x(0,t) = \Omega\, t$, $\theta_y(0,t) = 0$, and $\theta_z(0,t) = 0$. On the other hand, for $x = L$, one has $v(L,t) = 0$, and $w(L,t) = 0$.

The variational formulation presented in section 3.1, was made for a free-free beam, i.e. the above geometric boundary conditions were not considered. For this reason, they are included in the formulation as constraints, using the Lagrange multipliers method [25]. The details of this procedure are presented below.

Observe that the boundary conditions can be rewritten in matrix form as

$$[\mathscr{B}]\, \boldsymbol{Q}(t) = \boldsymbol{h}(t), \tag{70}$$

where the constraint matrix $[\mathscr{B}]$ is $8 \times N_{dofs}$ and has almost all entries equal to zero. The exceptions are $[\mathscr{B}]_{ii} = 1$ for $i = \{1, \cdots, 6\}$, $[\mathscr{B}]_{7(N_{dofs}-5)} = 1$, and $[\mathscr{B}]_{8(N_{dofs}-4)} = 1$. The constraint vector is given by

$$\boldsymbol{h}(t) = \begin{pmatrix} u(0,t) \\ v(0,t) \\ w(0,t) \\ \theta_x(0,t) \\ \theta_y(0,t) \\ \theta_z(0,t) \\ v(L,t) \\ w(L,t) \end{pmatrix}. \tag{71}$$

Making the change of basis defined by Eq.(64), one can rewrite Eq.(70) as

$$[B]\, \boldsymbol{q}(t) = \boldsymbol{h}(t), \tag{72}$$

where the $8 \times N_{red}$ reduced constraint matrix is defined by $[B] = [\mathscr{B}]\, [\Phi]$.

The discretization of Eq.(72) results in

$$[B]\, \boldsymbol{q}_{n+1} = \boldsymbol{h}_{n+1}, \tag{73}$$

where $\boldsymbol{h}_{n+1}$ is an approximation to $\boldsymbol{h}(t_{n+1})$. This equation defines the constraint that must be satisfied by the variational problem "approximate solution".

In what follows it is helpful to think that Eq.(69) comes from the minimization of an energy functional $\boldsymbol{q}_{n+1} \mapsto \mathscr{F}\left(\boldsymbol{q}_{n+1}\right)$, which is the weak form of this nonlinear system of algebraic equations.

Then, one defines the Lagrangian as

$$\mathscr{L}\left(\boldsymbol{q}_{n+1}, \boldsymbol{\lambda}_{n+1}\right) = \mathscr{F}\left(\boldsymbol{q}_{n+1}\right) + \boldsymbol{\lambda}_{n+1}^{T}\left([B]\,\boldsymbol{q}_{n+1} - \boldsymbol{h}_{n+1}\right), \quad (74)$$

being the (time-dependent) Lagrange multipliers vector of the form

$$\boldsymbol{\lambda}_{n+1} = \begin{pmatrix} \lambda_1(t_{n+1}) \\ \lambda_2(t_{n+1}) \\ \lambda_3(t_{n+1}) \\ \lambda_4(t_{n+1}) \\ \lambda_5(t_{n+1}) \\ \lambda_6(t_{n+1}) \\ \lambda_7(t_{n+1}) \\ \lambda_8(t_{n+1}) \end{pmatrix}. \quad (75)$$

Invoking the Lagrangian stationarity condition one arrives in the following $(N_{red}+8)\times(N_{red}+8)$ system of nonlinear algebraic equations

$$\begin{bmatrix} [\hat{K}] & [B]^{T} \\ [B] & [0] \end{bmatrix} \begin{pmatrix} \boldsymbol{q}_{n+1} \\ \boldsymbol{\lambda}_{n+1} \end{pmatrix} = \begin{pmatrix} \hat{\boldsymbol{f}}_{n+1} \\ \boldsymbol{h}_{n+1} \end{pmatrix}, \quad (76)$$

where $[0]$ is a 8×8 null matrix. The unknowns are $\boldsymbol{q}_{n+1}$ and $\boldsymbol{\lambda}_{n+1}$, and must be solved for each instant of time in the temporal mesh, in order to construct an approximation to the mechanical system dynamic response.

The solution of the nonlinear system of algebraic equations, defined by Eq.(76), is carried out first obtaining and solving a discrete Poisson equation for $\boldsymbol{\lambda}_{n+1}$ [22], and then using the first line of (76) to obtain $\boldsymbol{q}_{n+1}$. To solve these equations, a procedure of fixed point iteration is used in combination with a process of successive over relaxation [66].

5 Probabilistic modeling of system-parameter uncertainties

The mathematical model used to describe the physical behavior of the mechanical system is an abstraction of reality, and its use does not consider some aspects of the problem physics. Regarding the system modeling, either the beam theory used to describe the structure dynamics [41], as the friction and shock model used [26] are fairly established physical models, who have gone through several experimental tests to prove their validity, and have been used for many years in similar situations. On the other hand, the bit-rock interaction model adopted in this work, until now was used only in a purely numeric context [44], without any experimental validation. Thus, it is natural to conclude that bit-rock interaction law is the weakness of the model proposed in this work.

In this sense, this work will focus on modeling and quantifying the uncertainties that are introduced in the mechanical system by bit-rock interaction model. For convenience, it was chosen to use a parametric probabilistic approach [56], where only the uncertainties of system parameters are considered, and the maximum entropy principle is employed to construct the probability distributions.

5.1 Probabilistic framework

Let $\mathbb{X}$ be a real-valued random variable, defined on a probability space $(\Theta, \mathbb{\Sigma}, \mathbb{P})$, for which the probability distribution $P_{\mathbb{X}}(dx)$ on $\mathbb{R}$ admits a density $x \mapsto p_{\mathbb{X}}(x)$ with respect to dx. The support of the probability density function (PDF) $p_{\mathbb{X}}$ will be denoted by $\mathtt{Supp}\,\mathbb{X} \subset \mathbb{R}$. The mathematical expectation of $\mathbb{X}$ is defined by

$$\mathbb{E}\left[\mathbb{X}\right] = \int_{\mathtt{Supp}\,\mathbb{X}} x\, p_{\mathbb{X}}(x)\, dx\,, \quad (77)$$

and any realization of random variable $\mathbb{X}$ will be denoted by $\mathbb{X}(\theta)$ for $\theta \in \Theta$. Let $m_{\mathbb{X}} = \mathbb{E}\left[\mathbb{X}\right]$ be the mean value, $\sigma_{\mathbb{X}}^2 = \mathbb{E}\left[\left(\mathbb{X} - m_{\mathbb{X}}\right)^2\right]$ be the variance, and $\sigma_{\mathbb{X}} = \sqrt{\sigma_{\mathbb{X}}^2}$ be the standard deviation of $\mathbb{X}$. The Shannon entropy of $p_{\mathbb{X}}$ is defined by $\mathrm{S}\left(p_{\mathbb{X}}\right) = -\mathbb{E}\left[\ln p_{\mathbb{X}}(\mathbb{X})\right]$.

5.2 Probabilistic model for bit-rock interface law

Recalling that bit-rock interaction force and torque are, respectively, given by Eqs.(20) and (21), the reader can see that this bit-rock interface law is characterized by three parameters, namely, α_{BR}, $\mathit{\Gamma}_{\mathrm{BR}}$, and μ_{BR}. The construction of the probabilistic model for each one parameter of these parameters, which are respectively modeled by random variables $\mathbb{\alpha}_{\mathrm{BR}}$, $\mathbb{\Gamma}_{\mathrm{BR}}$, and $\mathbb{\mu}_{\mathrm{BR}}$, is presented below.

5.3 Distribution of force rate of change

As the rate of change α_{BR} is positive, it is reasonable to assume $\mathtt{Supp}\,\mathbb{\alpha}_{\mathrm{BR}} =]0, \infty[$. Therefore, the PDF of $\mathbb{\alpha}_{\mathrm{BR}}$ is a nonnegative function $p_{\mathbb{\alpha}_{\mathrm{BR}}}$, such that

$$\int_{\alpha=0}^{+\infty} p_{\mathbb{\alpha}_{\mathrm{BR}}}(\alpha)\, d\alpha = 1. \quad (78)$$

It is also convenient to assume that the mean value of $\mathbb{\alpha}_{\rm BR}$ is a known positive number, denoted by $m_{\mathbb{\alpha}_{\rm BR}}$, i.e.,

$$\mathbb{E}\left[\mathbb{\alpha}_{\rm BR}\right] = m_{\mathbb{\alpha}_{\rm BR}} > 0. \tag{79}$$

One also need to require that

$$\mathbb{E}\left[\ln\left(\mathbb{\alpha}_{\rm BR}\right)\right] = q_{\mathbb{\alpha}_{\rm BR}}, \quad |q_{\mathbb{\alpha}_{\rm BR}}| < +\infty, \tag{80}$$

which ensures, as can be seen in [53, 54, 55], that the inverse of $\mathbb{\alpha}_{\rm BR}$ is second order random variable. This condition is necessary to guarantee that the stochastic dynamical system associated to this random variable is of second order, i.e., it has finite variance. Employing the principle of maximum entropy one need to maximize the entropy function $\mathrm{S}\left(p_{\mathbb{\alpha}_{\rm BR}}\right)$, respecting the constraints imposed by (78), (79) and (80).

The desired PDF corresponds to the gamma distribution and is given by

$$p_{\mathbb{\alpha}_{\rm BR}}(\alpha) = \mathbb{1}_{]0,\infty[}(\alpha)\,\frac{1}{m_{\mathbb{\alpha}_{\rm BR}}}\left(\frac{1}{\delta^2_{\mathbb{\alpha}_{\rm BR}}}\right)^{1/\delta^2_{\mathbb{\alpha}_{\rm BR}}} \times\frac{1}{\Gamma(1/\delta^2_{\mathbb{\alpha}_{\rm BR}})}\left(\frac{\alpha}{m_{\mathbb{\alpha}_{\rm BR}}}\right)^{1/\delta^2_{\mathbb{\alpha}_{\rm BR}}-1}\exp\left(\frac{-\alpha}{\delta^2_{\mathbb{\alpha}_{\rm BR}}m_{\mathbb{\alpha}_{\rm BR}}}\right), \tag{81}$$

where the symbol $\mathbb{1}_{]0,\infty[}(\alpha)$ denotes the indicator function of the interval $]0,\infty[$, $0 \leq \delta_{\mathbb{\alpha}_{\rm BR}} = \sigma_{\mathbb{\alpha}_{\rm BR}}/m_{\mathbb{\alpha}_{\rm BR}} < 1/\sqrt{2}$ is a type of dispersion parameter, and

$$\Gamma(z) = \int_{y=0}^{+\infty} y^{z-1}\,e^{-y}\,dy, \tag{82}$$

is the gamma function.

5.4 Distribution of limit force

The parameter $\mathit{\Gamma}_{\rm BR}$ is also positive, in a way that $\mathtt{Supp}\,\mathbb{\Gamma}_{\rm BR} =]0,\infty[$, and consequently

$$\int_{\gamma=0}^{+\infty} p_{\mathbb{\Gamma}_{\rm BR}}(\gamma)\,d\gamma = 1. \tag{83}$$

The hypothesis that the mean is a known positive number $m_{\mathbb{\Gamma}_{\rm BR}}$ is also done, i.e.,

$$\mathbb{E}\left[\mathbb{\Gamma}_{\rm BR}\right] = m_{\mathbb{\Gamma}_{\rm BR}} > 0, \tag{84}$$

as well as that the technical condition, required for the stochastic dynamical system associated be of second order, is fulfilled, i.e.

$$\mathbb{E}\left[\ln\left(\mathbb{\Gamma}_{\rm BR}\right)\right] = q_{\mathbb{\Gamma}_{\rm BR}}, \quad |q_{\mathbb{\Gamma}_{\rm BR}}| < +\infty. \tag{85}$$

In a similar way to the procedure presented in section 5.3, it can be shown that PDF of maximum entropy is also gamma distributed, and given by

$$p_{\mathbb{\Gamma}_{\rm BR}}(\gamma) = \mathbb{1}_{]0,\infty[}(\gamma)\,\frac{1}{m_{\mathbb{\Gamma}_{\rm BR}}}\left(\frac{1}{\delta^2_{\mathbb{\Gamma}_{\rm BR}}}\right)^{1/\delta^2_{\mathbb{\Gamma}_{\rm BR}}} \times\frac{1}{\Gamma(1/\delta^2_{\mathbb{\Gamma}_{\rm BR}})}\left(\frac{\gamma}{m_{\mathbb{\Gamma}_{\rm BR}}}\right)^{1/\delta^2_{\mathbb{\Gamma}_{\rm BR}}-1}\exp\left(\frac{-\gamma}{\delta^2_{\mathbb{\Gamma}_{\rm BR}}m_{\mathbb{\Gamma}_{\rm BR}}}\right). \tag{86}$$

5.5 Distribution of friction coefficient

With respect to the parameter $\mu_{\rm BR}$, one know it is non-negative and bounded above by the unity. Thus, one can safely assume that $\mathtt{Supp}\,\mathbb{\mu}_{\rm BR} = [0,1]$, so that the normalization condition read as

$$\int_{\mu=0}^{1} p_{\mathbb{\mu}_{\rm BR}}(\mu)\,d\mu = 1. \tag{87}$$

The following two conditions are also imposed

$$\mathbb{E}\left[\ln\left(\mathbb{\mu}_{\rm BR}\right)\right] = q^1_{\mathbb{\mu}_{\rm BR}}, \quad |q^1_{\mathbb{\mu}_{\rm BR}}| < +\infty, \tag{88}$$

$$\mathbb{E}\left[\ln\left(1-\mathbb{\mu}_{\rm BR}\right)\right] = q^2_{\mathbb{\mu}_{\rm BR}}, \quad |q^2_{\mathbb{\mu}_{\rm BR}}| < +\infty, \tag{89}$$

representing a weak decay of the PDF of $\mathbb{\mu}_{\rm BR}$ in 0^+ and 1^- respectively [53, 54, 55]. Evoking again the principle of maximum entropy considering now as known information the constraints defined by (87), (88), and (89) one has that the desired PDF is given by

$$p_{\mathbb{\mu}_{\rm BR}}(\mu) = \mathbb{1}_{[0,1]}(\mu)\,\frac{\Gamma(a+b)}{\Gamma(a)\,\Gamma(b)}\,\mu^{a-1}\,(1-\mu)^{b-1}, \tag{90}$$

which corresponds to the beta distribution

The parameters a and b are associated with the shape of the probability distribution, and can be related with $m_{\mathbb{\mu}_{\rm BR}}$ and $\delta_{\mathbb{\mu}_{\rm BR}}$ by

$$a = \frac{m_{\mathbb{\mu}_{\rm BR}}}{\delta^2_{\mathbb{\mu}_{\rm BR}}}\left(\frac{1}{m_{\mathbb{\mu}_{\rm BR}}} - \delta^2_{\mathbb{\mu}_{\rm BR}} - 1\right), \tag{91}$$

and

$$b = \frac{m_{\mathbb{\mu}_{\mathrm{BR}}}}{\delta^2_{\mathbb{\mu}_{\mathrm{BR}}}} \left(\frac{1}{m_{\mathbb{\mu}_{\mathrm{BR}}}} - \delta^2_{\mathbb{\mu}_{\mathrm{BR}}} - 1 \right) \left(\frac{1}{m_{\mathbb{\mu}_{\mathrm{BR}}}} - 1 \right). \quad (92)$$

5.6 Stochastic nonlinear dynamical system

Due to the randomness of parameters $\mathbb{\alpha}_{\mathrm{BR}}$, $\mathbb{\Gamma}_{\mathrm{BR}}$, and $\mathbb{\mu}_{\mathrm{BR}}$, the mechanical system physical behavior is now described, for all θ in Θ, by the stochastic nonlinear dynamical system defined by

$$[M]\,\ddot{\mathbb{q}}(t,\theta) + [C]\,\dot{\mathbb{q}}(t,\theta) + [K]\,\mathbb{q}(t,\theta) = \mathbb{f}\left(\mathbb{q}, \dot{\mathbb{q}}, \ddot{\mathbb{q}}\right), \quad (93)$$

$$\mathbb{q}(0,\theta) = \boldsymbol{q}_0, \qquad \text{and} \qquad \dot{\mathbb{q}}(0,\theta) = \dot{\boldsymbol{q}}_0, \quad a.s. \quad (94)$$

where $\mathbb{q}(t)$ is the random reduced displacement vector, $\dot{\mathbb{q}}(t)$ is the random reduced velocity vector, and $\ddot{\mathbb{q}}(t)$ is the random reduced acceleration vector, and $\mathbb{f}$ is the random reduced nonlinear force vector.

The methodology used to calculate the propagation of uncertainties through this stochastic dynamical system is Monte Carlo (MC) method [29], employing a strategy of parallelization described in [13].

6 Numerical experiments and discussions

In order to simulate the mechanical system nonlinear dynamics, the physical parameters presented in Table 1 are adopted, as well as $L = 100\ m$, the rotational and axial velocities in x, respectively given by $\Omega = 2\pi\ rad/s$, and $V_0 = 1/180\ m/s$. The values of these parameters do not correspond exactly to actual values used in a real drillstring, but are of the same order of magnitude. For this configuration, the beam geometry is discretized by 500 finite elements, and the interval of integration $[t_0, t_f] = [0, 10]\ s$ is considered.

For the friction and shock model constants, are considered the values shown in Table 2, which have order of magnitude typical of a borehole wall made of steel [67].The low value for μ_{FS} is justified by the fact that, in a real system, there is a fluid between the column and borehole wall, which carries a substantial reduction in the torsional friction.

The bit-rock interaction model constants can be seen in Table 3, and were estimated following a similar strategy as that shown in [44].

Table 1 Physical parameters of the mechanical system that are used in the simulation.

parameter	value	unit
ρ	7900	kg/m^3
g	9.81	m/s^2
ν	0.3	—
κ_s	6/7	—
c	0.01	—
E	203×10^9	Pa
R_{bh}	95×10^{-3}	m
R_{int}	50×10^{-3}	m
R_{ext}	80×10^{-3}	m

Table 2 Parameters of the friction and shock model that are used in the simulation.

parameter	value	unit
k_{FS_1}	1×10^{10}	N/m
k_{FS_2}	1×10^{16}	N/m^3
c_{FS}	1×10^6	$(N/m^3)/(m/s)$
μ_{FS}	0.25	—

Table 3 Parameters of the bit-rock interaction model that are used in the simulation.

parameter	value	unit
Γ_{BR}	30×10^3	N
α_{BR}	400	$1/(m/s)$
μ_{BR}	0.4	—

6.1 "Validation" of the computational model

In order to validate to computational model developed in this work, the most widely accepted approach would be through comparison with experimental data [36]. Unfortunately, it is very difficult to obtain such experimental measurements for the type of mechanical system analyzed in this work. Accordingly, as in many analyzes of dynamic systems with complex behavior (e.g. aerospace, automotive, etc), this work used numerical simulation without experimental analysis. However, it is clear that such numerical simulations do have meaning, and are only useful, if prior validation of models, formulations, and numerical simulation software were obtained. In the cases treated, "validations" of the model, formulation, and software were obtained, step by step, by comparing the results obtained with the software with the following reference results: (i) linear static; (ii) nonlinear static with contact; (iii) linear dynamic nonrotating without contact; (iv) linear dynamic rotating without contact; (v) nonlinear nonrotating dynamic with contacts (shocks); and (vi) nonlinear rotating dynamic with contacts (shocks). All tests were performed and the analyzes were used to "validate" the model, the formulation, and the results of numerical simulations.

6.2 Modal analysis of the mechanical system

In this section, the modal content of the mechanical system is investigated. This investigation aims to identify the natural frequencies of the system, and, especially, to check the influence of *slenderness ratio*, defined as the ratio between beam length and external diameter, in the natural frequencies distribution.

Therefore, the dimensionless frequency band for the problem is assumed as being $B = [0, 4]$, with the dimensionless frequency defined by

$$f^* = \frac{f\,L}{c_L}, \tag{95}$$

where f is the dimensional frequency (Hz), and $c_L = \sqrt{E/\rho}$ is the longitudinal wave velocity. Once it was defined in terms of a dimensionless frequency, the band of analysis does not change when the beam length is varied. Also, the reader can check that this band is representative for the mechanical system dynamics, once the beam rotates at 2π rad/s, which means that it is excited at 1 Hz.

In Figure 10 one can see the distribution of the flexural modes as a function of dimensionless frequency, for several values of slenderness ratio. Clearly it is observed that the flexural modes are denser in the low frequency range. Further, when the slenderness ratio increases, the modal density in the low frequencies range tend to increase.

A completely different behavior is observed for the torsional and longitudinal (traction-compression) modes of vibration, as can be seen in Figures 11 and 12, respectively. One can note that, with respect to these two modes of vibration, the modal distribution is almost uniform with respect to dimensionless frequency, and invariant to changes in the slenderness ratio.

It may also be noted from Figures 10 to 12 that lowest natural frequencies are associated with flexural mechanism. This is because beam flexural stiffness is much smaller than torsional stiffness, which, in turn, is less than axial stiffness. In other words, it is much easier to bend the beam than twisting it. However, twists the beam is easier than buckling it.

The dimensionless frequency band adopted in the analysis corresponds to a maximum dimensional frequency of $f_{max} = 4\,c_L/L$. In this way, a nominal time step of $\Delta t = (2\,f_{max})^{-1}$ is adopted for time integration. This time step is automatically refined by the algorithm of integration, whenever necessary, to capture the shock effects.

6.3 Construction of the reduced model

In the reduced model construction, are taken into account the mechanical system rigid body modes, as well as the modes of bending, torsion and traction-compression. The construction strategy consists of including: (i) the two rigid body modes (translation and rotation); (ii) all flexural modes such that $0 < f^* \leq 5\,L/c_L$; (iii) all torsional modes such that $0 < f^* \leq 4$; (iv) all longitudinal modes such that $0 < f^* \leq 4$.

In this way, the total number of modes used in FEM model is a function of beam length. In Table 4 the reader can see a comparison, for different values of L, of the full FEM model dimension and the corresponding reduced order model dimension. Note that using the above strategy, the reduced model dimension is always much smaller than the full model dimension.

Table 4 Dimension of the FEM model as a function of beam length.

beam length (m)	full model DoFs	reduced model DoFs
50	306	37
100	3006	49
150	4506	60

6.4 Calculation of static equilibrium configuration

Before the beginning of drilling operation, the drillstring is inserted into the borehole, without axial velocity and rotation imposed. Due to gravitational effects, the column deflects until it reaches a static equilibrium configuration. This configuration can be calculated by temporal integration of the dynamical system defined by Eqs.(65) and (66), assuming zero initial conditions, i.e., $\Omega = 0$ rad/s, and $V_0 = 0$ m/s. In this way, after a short transient, the system reaches static equilibrium and remains in this configuration indefinitely.

An illustration of this equilibrium configuration, for a 100 m long column is presented in Figure 13. In this illustration, one can see the mechanical system sectioned by the plane $y = 0$ m, as well as by the planes $x = \{0, 50, 100\}$ m. A visual inspection clearly indicates that this equilibrium is stable. Moreover, as this equilibrium configuration is the initial state of a real system, it will be used as initial condition in all other simulations reported bellow.

An animation which illustrates the beam static equilibrium calculation can be seen in Online Resource 1.

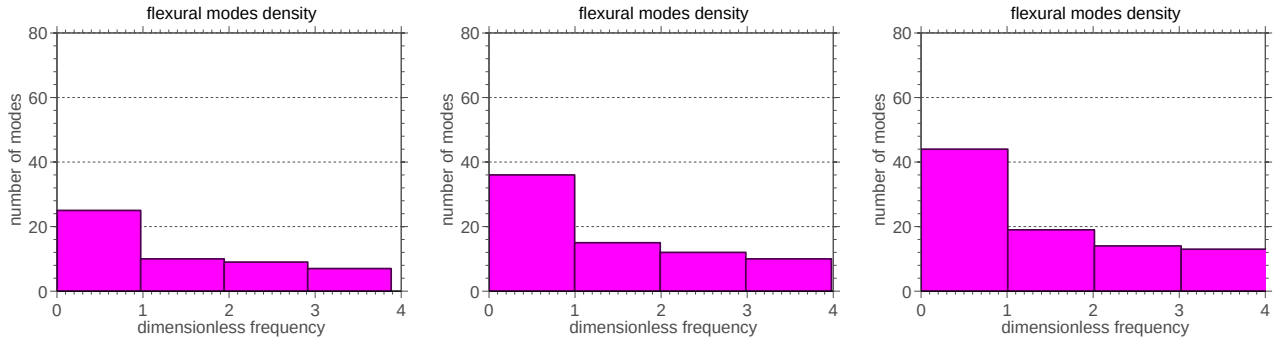

(a) slenderness = 312.5 (b) slenderness = 625.0 (c) slenderness = 937.5

Fig. 10 Distribution of the flexural modes as function of dimensionless frequency, for several values of slenderness ratio.

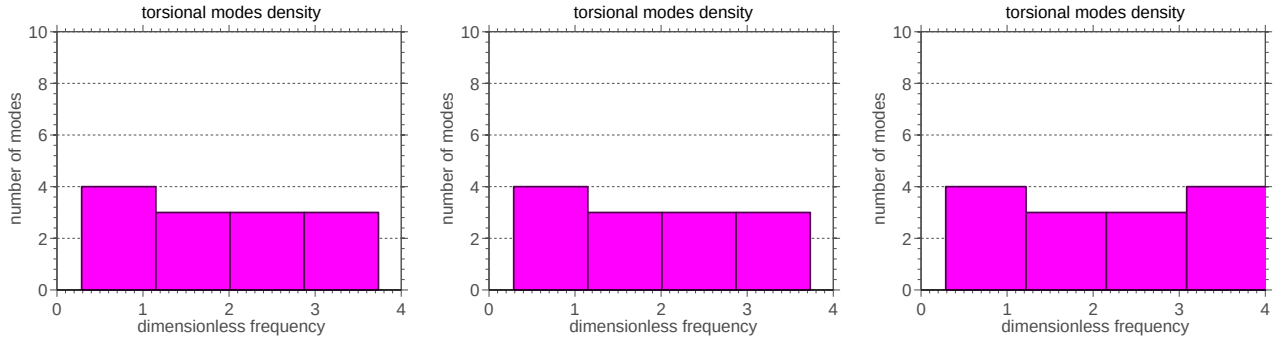

(a) slenderness = 312.5 (b) slenderness = 625.0 (c) slenderness = 937.5

Fig. 11 Distribution of the torsional modes as function of dimensionless frequency, for several values of slenderness ratio.

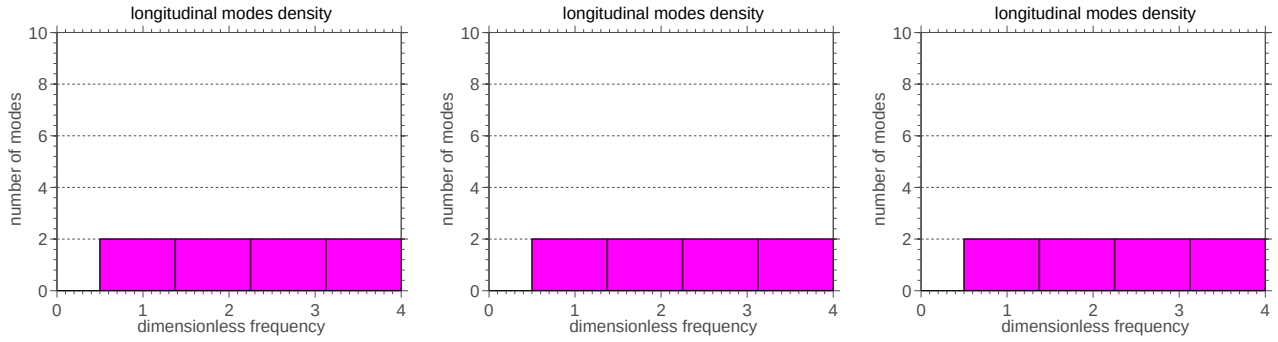

(a) slenderness = 312.5 (b) slenderness = 625.0 (c) slenderness = 937.5

Fig. 12 Distribution of the longitudinal modes as function of dimensionless frequency, for several values of slenderness ratio.

6.5 Drill-bit nonlinear dynamic behavior

The drill-bit longitudinal displacement and velocity, can be seen in Figure 14. For practical reasons, some scaling factors were introduced in the units of measure of these quantities. They allow one to read the displacement in "millimeter", and the velocity in "meters per hour". Accordingly, it is noted that, during the interval of analysis, the column presents an advance in forward direction with very small axial oscillations for displacement. The axial oscillations for velocity curve are more pronounced, and correspond to the vibration mechanism known as *bit-bounce*, where the drill-bit loses contact with the soil and then hits the rock abruptly. This phenomenon, which is widely observed in real systems [60], presents itself discreetly in the case analyzed. Note that the velocity exhibits a mean value of 19.36 "meters per hour", close to the velocity $V_0 = 20$ "meters per hour", which is imposed on the beam left end. Also, throughout the "temporal window" analyzed, one can observe packages where the drill-bit velocity presents

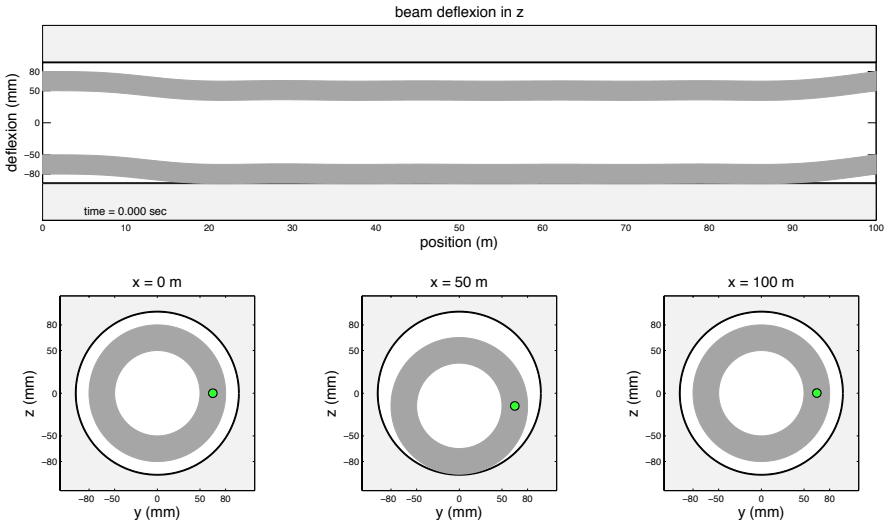

Fig. 13 Illustration of static equilibrium configuration of a horizontal drillstring with 100 m length.

large fluctuations, which can reach up to 40 times the mean value.

The drill-bit rotation and angular velocity, can be seen in Figure 15. Now the scale factors allow one to read rotation in "revolution", and angular velocity in "revolution per minute". Thus, what is observed is a almost monotonic rotation. However, when one looks to the angular velocity, it is possible to see packages of fluctuations with amplitude variations that can reach up to an order of magnitude. This indicates that drill-bit undergoes a blockage due to torsional friction, and then it is released subtly, so that its velocity is sharply increased, in a *stick-slip* phenomenon type. This is also seen experimentally [60] in real drilling systems, and a serious consequence of this blockage is the reduction of drilling process efficiency.

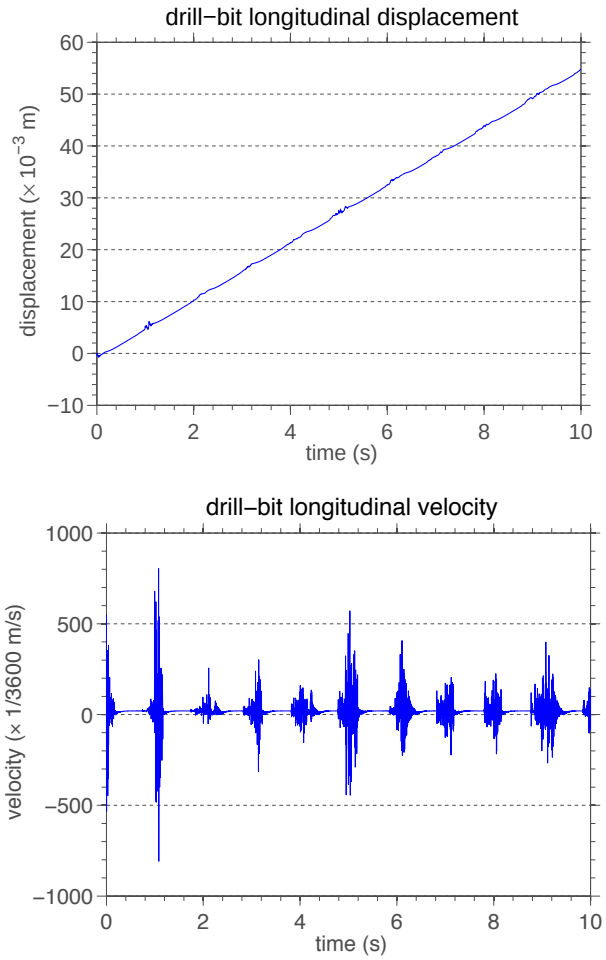

Fig. 14 Illustration of drill-bit displacement (top) and drill-bit velocity (bottom).

6.6 Transverse nonlinear dynamics of the beam

Observing the beam cross section at $x = 50\ m$, for which transversal displacement (top) and velocity (bottom) are shown in Figure 16, one can see an asymmetry of the displacement, with respect to the plane $z = 0\ m$. This is due to gravity, which favors the beam to move below this plane. Furthermore, one can note that this signal is composed of "packages", which has a recurring oscillatory pattern. As will be seen in section 6.7, these packages present a strong correlation with the number of impacts which the mechanical system is subjected.

The evolution of the beam cross-section radial displacement, for $x = 50\ m$, can be seen in Figure 17, which shows that several transverse impacts occur between drillstring and borehole wall during the drilling

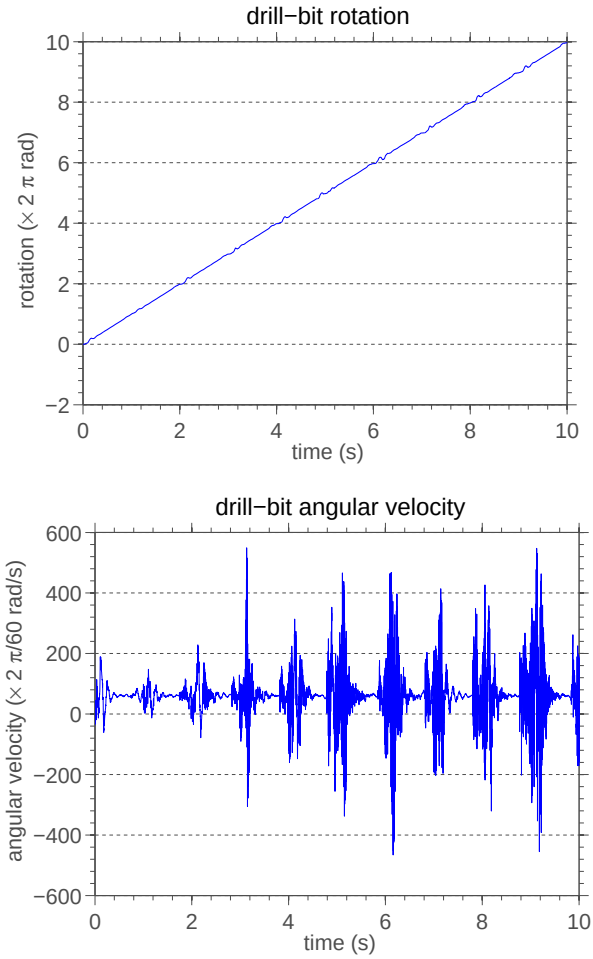

Fig. 15 Illustration of drill-bit rotation (top) and drill-bit angular velocity (bottom).

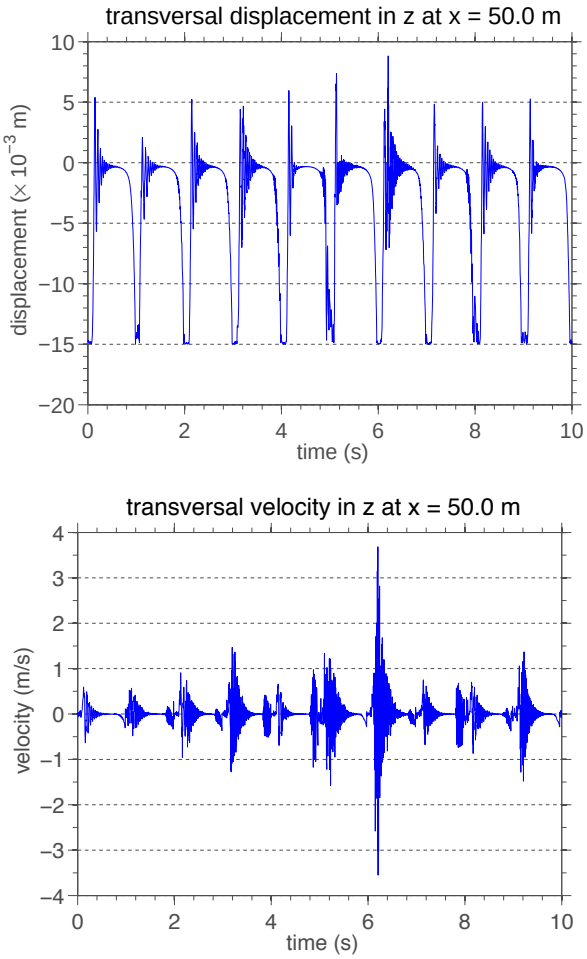

Fig. 16 Illustration of transversal displacement (top) and velocity in z (bottom) when $x = 50\ m$.

process. This fact is also reported experimentally [60], and is an important cause of damage for both, well and drillstring.

Note that, after an impact, the oscillations amplitudes decreases until subtly increase sharply, giving rise to a new impact, and then the entire process repeats again.

6.7 Influence of transverse impacts on the nonlinear dynamics

In Figure 18 it is shown the map $t \in \mathbb{R} \mapsto$ `number of shocks` $\in \mathbb{N}$, which associates for any instant t the number of impacts suffered by the mechanical system.

The "packages of fluctuation" observed in Figures 14 to 16 correspond to transitory periods of the dynamical system, and are highly correlated with the process of collision between beam and borehole wall. This assertion can be verified if the reader compares the graphs of Figures 14 to 16 with the graph of Figure 18, which shows the existence of "shock packages". The existence of a correlation is clearly evident.

Whenever there is a shock, the system "loses it memory" about previous dynamic behavior, and undergoes a new transient period until reach a steady state again. This behavior is repeated 11 times in the "temporal window" analyzed.

Regarding the distribution of impacts along the beam, the map $x \in [0, L] \mapsto$ `number of shocks` $\in \mathbb{N}$, which associates for any position x the number of impacts suffered by the mechanical system, is shown in Figure 19. It is clear that impacts do not occur near the beam ends. This is natural due to the restrictions of movement imposed by the boundary conditions.

The impacts between drillstring and borehole wall generate nonlinear elastic deformations in the beam, but without residual deformation effects. In this contact also occurs energy dissipation, due to the normal shock, and the torsional friction induced by beam rotation. These mechanical contacts also activate flexural modes

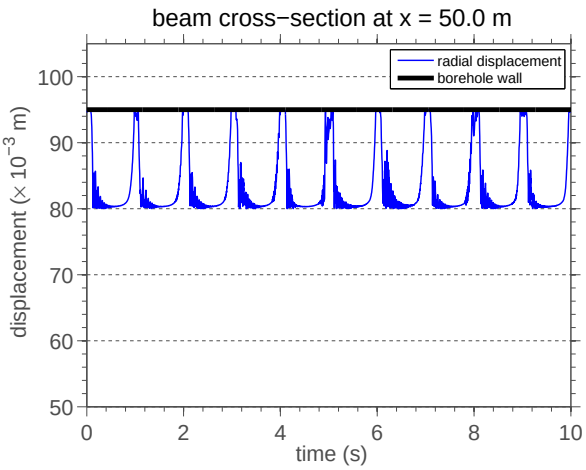

Fig. 17 Illustration of beam radial displacement for $x = 50\ m$.

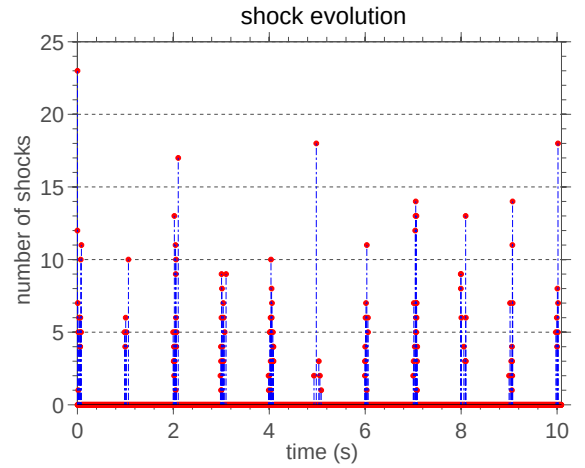

Fig. 18 Illustration of the number of impacts suffered by the mechanical system as function of time.

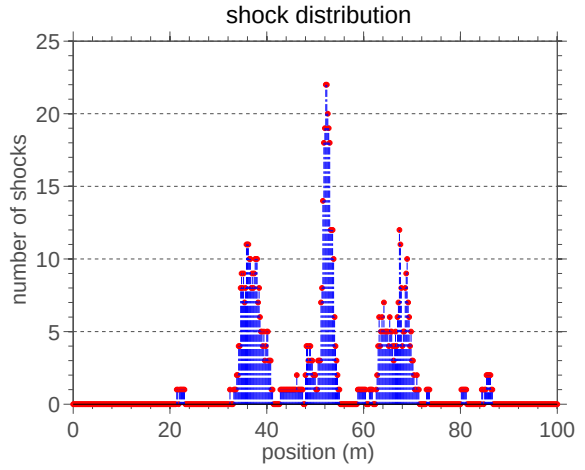

Fig. 19 Illustration of the number of impacts suffered by the mechanical system as function of position.

of vibration associated to high natural frequencies, so that the mechanical system assumes complex spatial configurations, as can be seen, for several instants, in Figure 20.

It is also very clear from Figure 20 that, the mechanical contacts between beam and borehole wall, do not occur all the time among discrete points, they can also be seen along continuous line segments.

For a qualitative illustration of the nonlinear dynamics, the reader can see Online Resource 2.

6.8 Spectral analysis of the nonlinear dynamics

All signals presented above, that are associated with the mechanical system response, have stochastic characteristics. Thereby, for a good understanding of them, it is necessary to analyze their spectral content through the power spectral density (PSD) function [37].

The PSDs that are presented in this section (magenta line) were estimated using the periodogram method [37], and the smooth curves (blue line) appearing were obtained by a filtering process, using a Savitzky-Golay filter [48]. The PSDs are measured in dB/Hz, where the intensity of reference is adopted as being equal to one.

An illustration of PSD functions of drill-bit velocity and angular velocity is show in Figure 21. One can note that, for velocity, the two peaks of highest amplitude correspond to the frequencies 84.55 Hz, and 115.20 Hz, respectively. These frequencies are very close to the flexural frequencies 83.65 Hz, and 114.27 Hz, so that drill-bit axial dynamics is controlled by the transversal mechanisms of vibration. Furthermore, with respect to angular velocity, it is noted a peak standing out in relation to the others. This peak is associated with 7.92 Hz frequency, which is very close to the flexural frequency 7.63 Hz.

In Figure 22 the reader can see an illustration of PSD functions of beam transversal velocity in z and angular velocity around x when $x = 50\ m$. The two peaks of highest amplitude, for velocity in z, correspond to the frequencies 143.20 Hz, and 172.50 Hz, respectively. These frequencies are close to the flexural frequencies 144.94 Hz, and 174.07 Hz, which indicates that lateral vibrations in z, when $x = 50\ m$, are induced by the transversal vibration mechanism. In addition, in what concerns angular velocity around x, the two peaks of largest amplitude are associated to the frequencies 6.93 Hz, and 107.10 Hz, respectively close to the flexural frequencies 6.59 Hz, and 106.18 Hz.

According to Figure 23, flexion is the primary mechanism of vibration that causes beam and borehole wall impacts, since the highest peak of the PSD shown in this

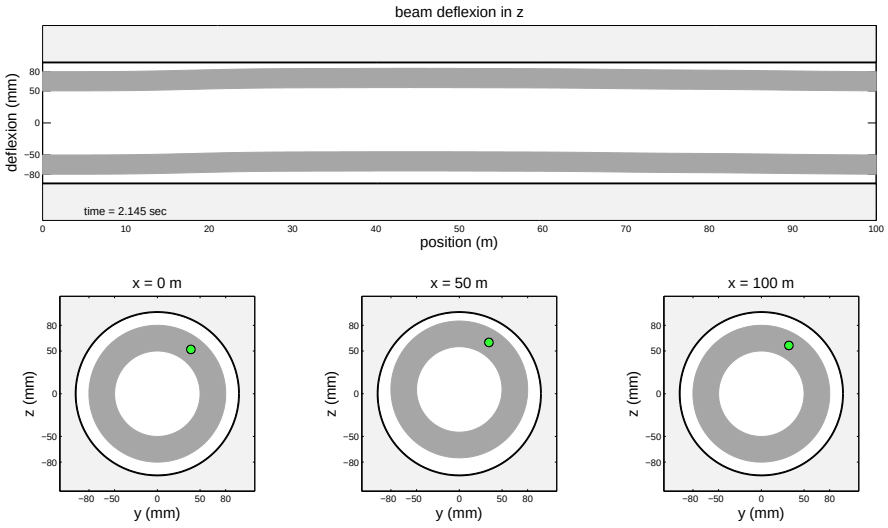

(a) $t = 2.145\ s$

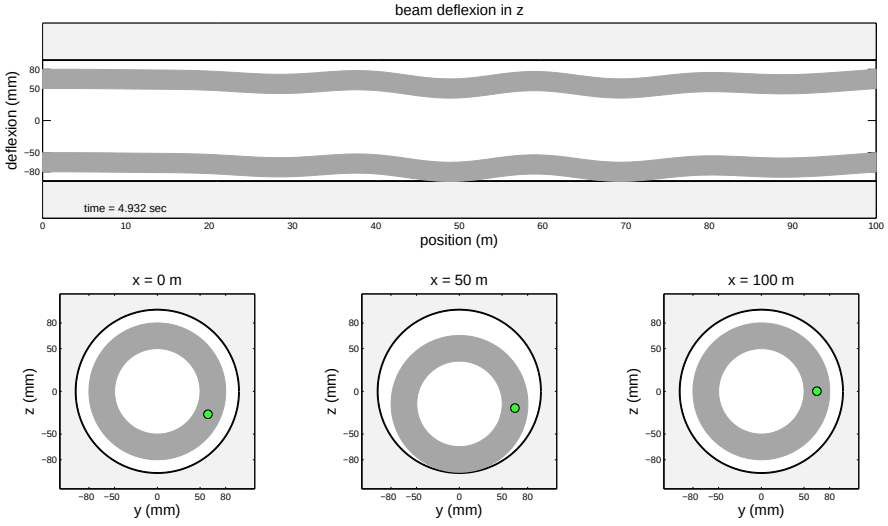

(b) $t = 4.932\ s$

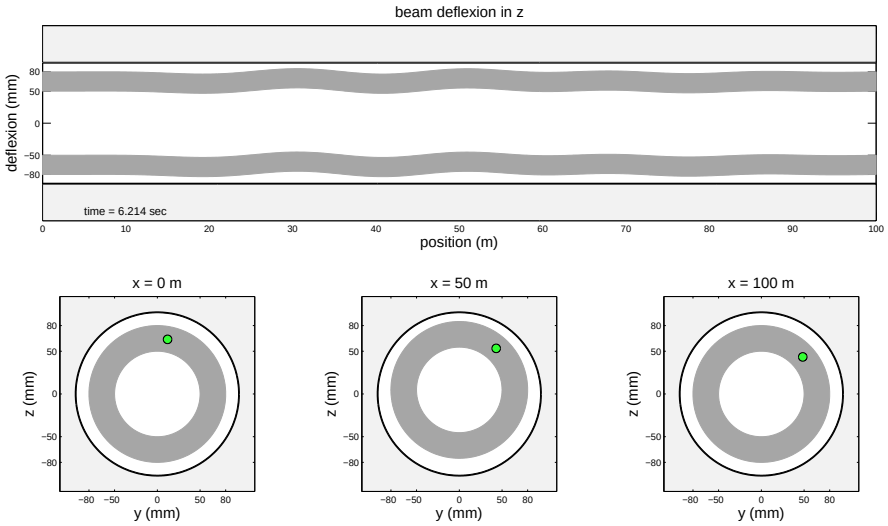

(c) $t = 6.214\ s$

Fig. 20 Illustration of the mechanical system, for several instants, sectioned by the planes $y = 0\ m$, and $x = \{0, 50, 100\}\ m$.

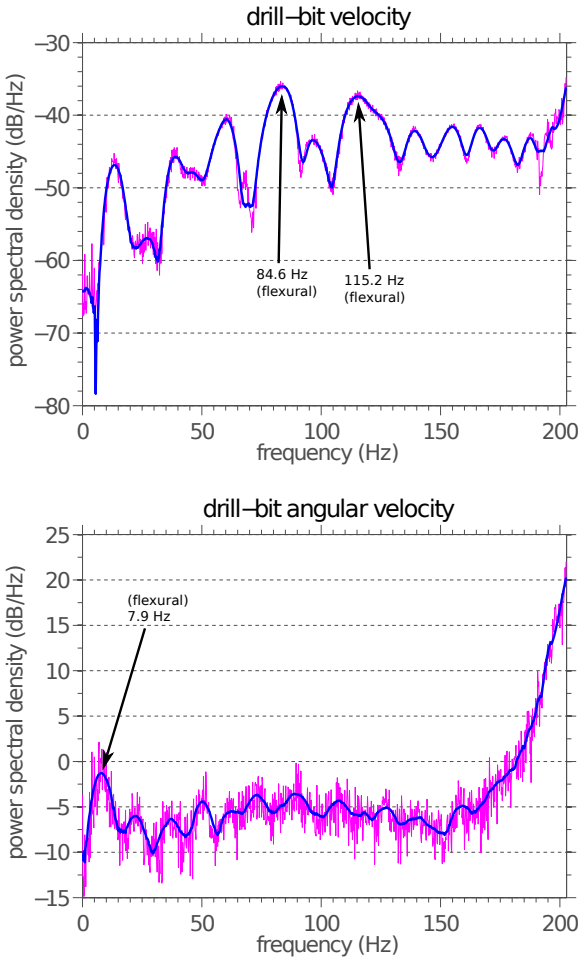

Fig. 21 Illustration of power spectral density functions of drill-bit velocity (top) and angular velocity (bottom).

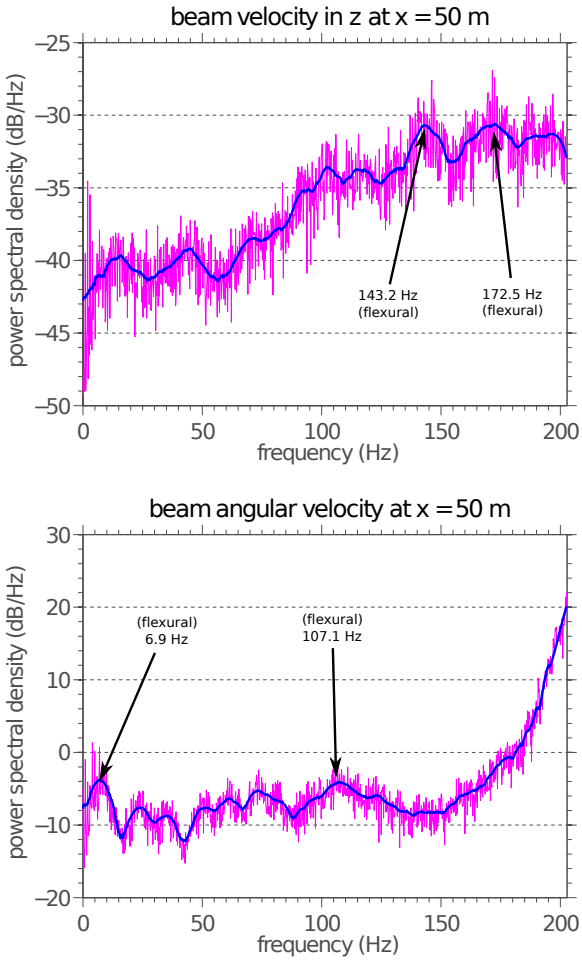

Fig. 22 Illustration of power spectral density functions of beam transversal velocity in z (top) and angular velocity around x (bottom) when $x = 50\ m$.

figure is associated with frequency 57.42 Hz, which is close to the flexural frequency 57.77 Hz. This result is consistent with the intuition and with what is reported in the literature of drillstrings in vertical configuration [60].

6.9 Analysis of drilling process efficiency

The drilling process efficiency is defined as

$$\mathcal{E} = \frac{\int_{t_0}^{t_f} \mathcal{P}_{out}\, dt}{\int_{t_0}^{t_f} \mathcal{P}_{in}\, dt}, \tag{96}$$

where $\mathcal{P}_{out}$ is the useful (output) power used in the drilling process, and $\mathcal{P}_{in}$ is the total (input) power injected in the system. The output power is due to drill-bit movements of translation and rotation so that

$$\mathcal{P}_{out} = \dot{u}_{bit}^{+}\,(-F_{\text{BR}})^{+} \;+\; \omega_{bit}^{+}\,(-T_{\text{BR}})^{+}\,, \tag{97}$$

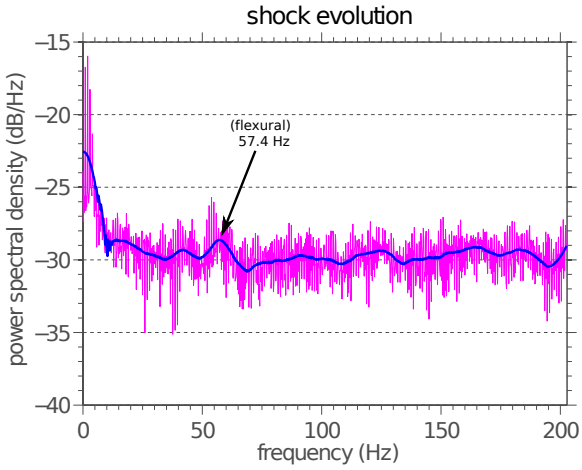

Fig. 23 Illustration of power spectral density function of number of shocks per unit of time.

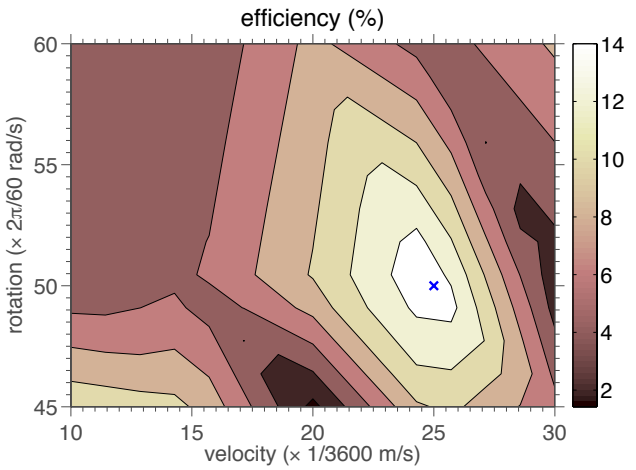

Fig. 24 Illustration of efficiency function contour plot, for an "operating window" defined by $1/360\ m/s \leq V_0 \leq 1/120\ m/s$ and $3\pi/2\ rad/s \leq \Omega \leq 2\pi\ rad/s$. The maximum is indicated with a blue cross.

where the upper script $^+$ means the function positive part. The input power is defined as

$$\mathcal{P}_{in} = \dot{u}(0,t)^+ (-\lambda_1)^+ \ + \ \dot{\theta}_x(0,t)^+ (-\lambda_4)^+, \tag{98}$$

where the first and the fourth Lagrange multipliers, respectively, represent the drilling force and torque on the beam origin. The reason for considering, in the above definitions, only functions positive part is that negative powers do not contribute to the drilling process.

One can observe the contour map of $\mathcal{E}$, for an "operating window" defined by $1/360\ m/s \leq V_0 \leq 1/120\ m/s$ and $3\pi/2\ rad/s \leq \Omega \leq 2\pi\ rad/s$, in Figure 24. Note that, by operating window of a drillstring, one means the subset of $\mathbb{R}^2$ that provides acceptable values for the pair (Ω, V_0). In order to facilitate the results interpretation, some scaling factors were introduced in the units of measure. They allow one to read velocity in "meters per hour" and rotation in "rotation per minute".

Accordingly, it can be noted in Figure 24 that the optimum operating condition is obtained at the point $(V_0, \Omega) = (1/144\ m/s, 5\pi/3\ rad/s)$, which is indicated with a blue cross in the graph. This point corresponds to an efficiency of approximately 16%. Suboptimal operation conditions occur in the vicinity of this point, and some points near the "operating window" boundary show lower efficiency.

6.10 Optimization of drillstring rate of penetration

In order to optimize the drilling process of an oil well in horizontal configuration, it is necessary to maximize the drillstring ROP into the soil.

The instantaneous rate of penetration is given by the function $\dot{u}_{bit}(t)$, defined for all instants of analysis. Meanwhile, only contributes to the column advance, the positive part of this function $\dot{u}^+_{bit}(t)$. In addition, as objective function, it is more convenient to consider a scalar function. Thus, the temporal mean of $\dot{u}^+_{bit}(t)$ is adopted as rate of penetration, and, consequently, objective function of the optimization problem

$$\texttt{rop}(\Omega, V_0) = \frac{1}{t_f - t_0} \int_{t=t_0}^{t_f} \dot{u}^+_{bit}(t)\, dt. \tag{99}$$

Furthermore, respect the material structural limits is indispensable to avoid failures in drillstring during the drilling process. For this reason, von Mises criterion of failure is considered, where it is established that, for all pairs (Ω, V_0) in the "operating window", one has

$$\texttt{UTS} - \max_{\substack{0\leq x\leq L \\ t_0\leq t\leq t_f}} \left\{\sigma_{VM}(V_0, \Omega, x, t)\right\} \geq 0, \tag{100}$$

where UTS is the material ultimate tensile strength, and σ_{VM} is the von Mises equivalent stress.

Regarding the rate of penetration analysis, "operating window" is defined by the inequations $1/360\ m/s \leq V_0 \leq 1/90\ m/s$ and $3\pi/2\ rad/s \leq \Omega \leq 7\pi/3\ rad/s$, and $\texttt{UTS} = 650 \times 10^6\ Pa$.

The contour map of constraint (100), is shown in Figure 25. From the way (100) is written, the Mises criterion is not satisfied when the function is negative, which occurs in a "small neighborhood" of the upper left corner of the rectangle that defines the "operating window". It is noted that all other points respect the material structural limits. In this way, then, the "operating window" *admissible* region consists of all points that satisfy the constraint.

In Figure 26 the reader can see the contour map of rop function. Taking into account only points in the admissible region, the maximum of rop occurs at $(V_0, \Omega) = (7/720\ m/s, 2\pi\ rad/s)$, which is indicated on the graph with a blue cross. This point corresponds to a mean rate of penetration, during the time interval analyzed, approximately equal to 90 "meters per hour".

It is worth remembering that the definition of rop uses temporal mean of $\dot{u}_{bit}(t)$ positive part. In such a way, it is not surprising to find the maximum value of rop much higher than the corresponding velocity, V_0 imposed on the column left end. This occurs because, by taking only the function positive part, the rate of penetration value increases.

To see how significant is the inclusion of $\dot{u}_{bit}(t)$ positive part in the definition of rop, the reader can see Figure 27. This figure shows the same information as

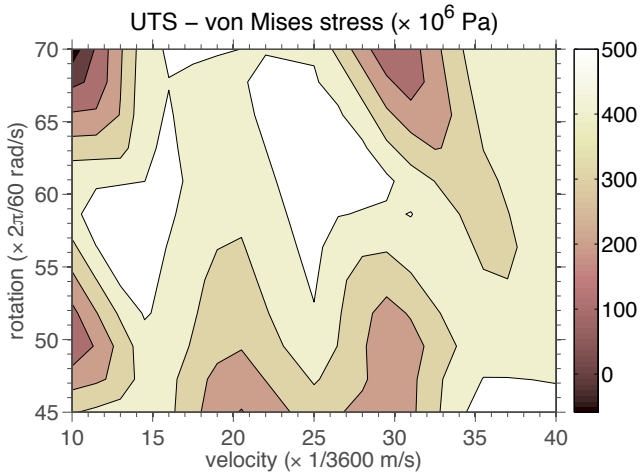

Fig. 25 Illustration of maximum von Mises stress contour plot, for an "operating window" defined by $1/360\ m/s \leq V_0 \leq 1/90\ m/s$ and $3\pi/2\ rad/s \leq \Omega \leq 7\pi/3\ rad/s$.

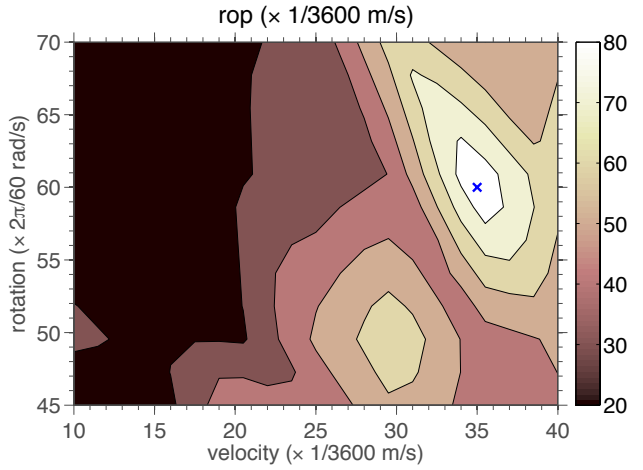

Fig. 26 Illustration of rate of penetration function contour plot, for an "operating window" defined by $1/360\ m/s \leq V_0 \leq 1/90\ m/s$ and $3\pi/2\ rad/s \leq \Omega \leq 7\pi/3\ rad/s$. The maximum is indicated with a blue cross.

Figure 26, i.e., the contour map of `rop` function, but now considering $\dot{u}_{bit}(t)$ instead of $\dot{u}^{+}_{bit}(t)$ in the definition of `rop`. Note that, in comparison with the contour map of Figure 26, lower values for the function levels are observed, and these values now are closer to V_0. Furthermore, the topology of contour lines change, so that no local extreme point can be seen isolated. This example shows the importance of considering $\dot{u}^{+}_{bit}(t)$ in the definition of `rop`.

6.11 Probabilistic analysis of the dynamics

For the probabilistic analysis of the dynamic system a parametric approach is used, where the random parameters distributions are constructed according to the

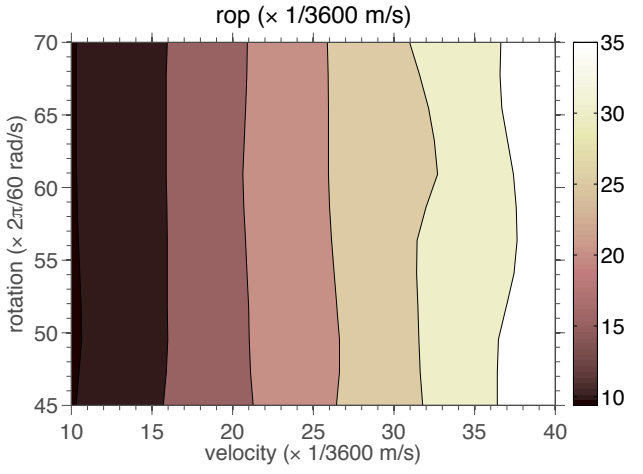

Fig. 27 Illustration of the contour plot of the rate of penetration function, with an alternative definition, for an "operating window" defined by $1/360\ m/s \leq V_0 \leq 1/90\ m/s$ and $3\pi/2\ rad/s \leq \Omega \leq 7\pi/3\ rad/s$.

procedure presented in section 5. In this case, the random variables of interest are characterized by the mean values $m_{\alpha_{\mathrm{BR}}} = 400\ 1/m/s$, $m_{\Gamma_{\mathrm{BR}}} = 30 \times 10^3\ N$, and $m_{\mu_{\mathrm{BR}}} = 0.4$, and the dispersion factors $\delta_{\alpha_{\mathrm{BR}}} = 0.5\%$, $\delta_{\Gamma_{\mathrm{BR}}} = 1\%$, and $\delta_{\mu_{\mathrm{BR}}} = 0.5\%$.

To compute the parameters uncertainties propagation through the model, MC method is employed. To analyze the convergence of MC simulations, it is taken into consideration the map $n_s \in \mathbb{N} \mapsto \mathtt{conv}_{\mathrm{MC}}(n_s) \in \mathbb{R}$, being

$$\mathtt{conv}_{\mathrm{MC}}(n_s) = \left(\frac{1}{n_s} \sum_{n=1}^{n_s} \int_{t=t_0}^{t_f} \left\| \mathfrak{q}(t,\theta_n) \right\|^2 \, dt \right)^{1/2}, \quad (101)$$

where n_s is the number of MC realizations, and $\|\cdot\|$ denotes the standard Euclidean norm. This metric allows one to evaluate the approximation $\mathfrak{q}(t,\theta_n)$ convergence in mean-square sense. For further details the reader is encouraged to see [55].

The evolution of $\mathtt{conv}(n_s)$ as function of n_s can be seen in Figure 28. Note that for $n_s = 1024$ the metric value has reached a steady value. In this sense, if something is not stated otherwise, all the stochastic simulations that follows in this work use $n_s = 1024$.

An illustration of the mean value (blue line), and a confidence band (grey shadow), wherein a realization of the stochastic dynamic system has 95% of probability of being contained, for drill-bit longitudinal displacement and velocity is shown in Figure 29. For sake of reference, the deterministic model, which the numerical results were presented earlier, is also shown and called nominal model (red line). It is observed that for

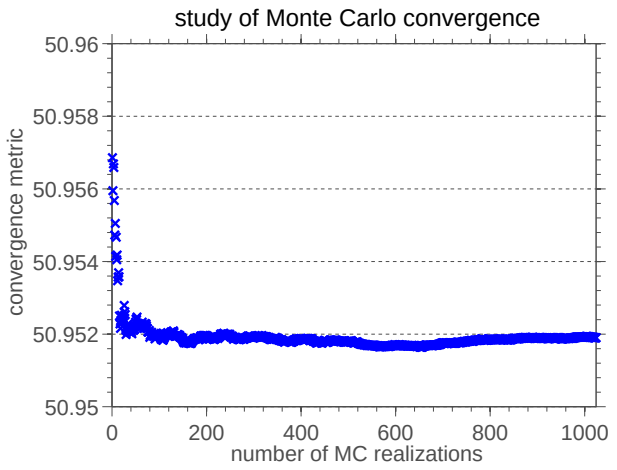

Fig. 28 This figure illustrates the convergence metric of MC simulation as function of the number of realizations.

the displacement, mean value and nominal model are very similar. Meanwhile, for the velocity, mean value presents oscillations that are correlated with the nominal model, but with very different amplitudes. Regarding the confidence band, there are significant amplitudes in the instants that corresponds to the fluctuation packages, and negligible amplitudes in the other moments.

Fixing time in $t = 10\ s$, it is possible to analyze the behavior of drill-bit longitudinal velocity through its normalized PDF, which is presented in Figure 30. In this context normalized means a distribution of probability with zero mean and unit standard deviation. It is observed an unimodal behavior, with maximum value occurring in a neighborhood of the mean value, with small dispersion around this position.

In Figure 31, the reader can see the nominal model, the mean value, and the 95% probability envelope of drill-bit rotation and angular velocity. A good agreement between rotation nominal model and mean value is observed, and the confidence band around it is negligible. On the other hand, with respect to the angular velocity, it is possible to see discrepancies in the nominal model and mean value amplitudes. These differences occur in the instants when the system is subject to shocks, as in the case of drill-bit longitudinal velocity. The band of uncertainty shows that the dispersion around mean value increases with time, due to accumulation of uncertainties, but also in reason of the impacts, once its amplitude increases a lot near the instants where the mean value presents large fluctuations, i.e., the instants which are correlated with the beam and borehole wall impacts.

For $t = 10\ s$, the reader can see the normalized PDF of drill-bit angular velocity in Figure 32. It is noted

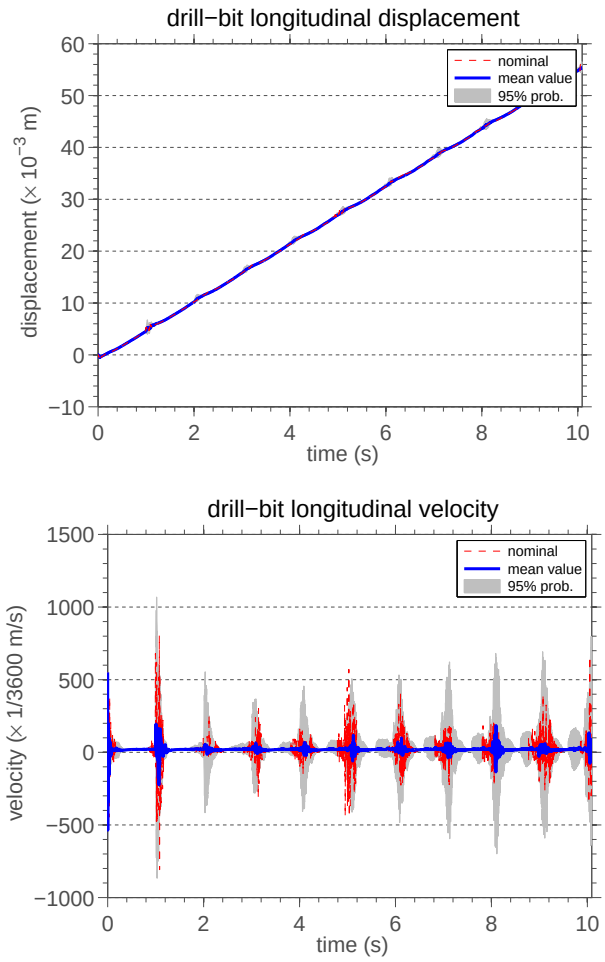

Fig. 29 Illustration of the nominal model (red line), the mean value (blue line), and the 95% probability envelope (grey shadow) for the drill-bit longitudinal displacement (top) and velocity (bottom).

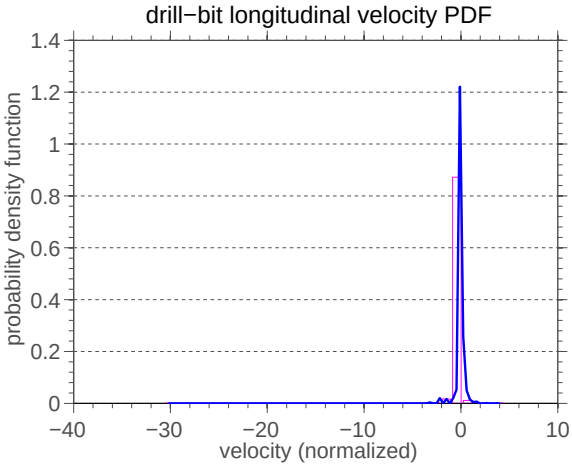

Fig. 30 Illustration of the normalized probability density function of drill-bit longitudinal velocity.

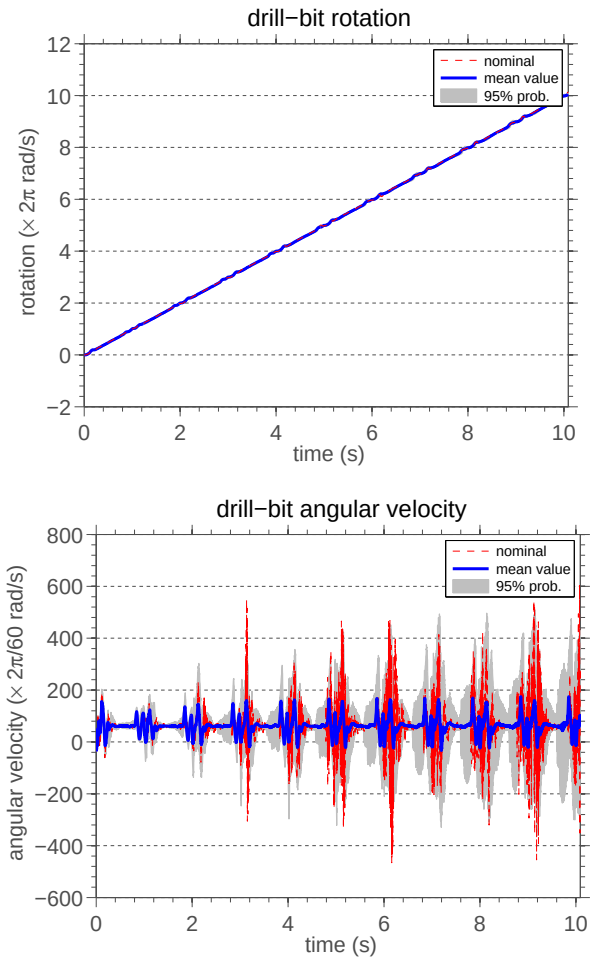

Fig. 31 Illustration of the nominal model (red line), the mean value (blue line), and the 95% probability envelope (grey shadow) for the drill-bit rotation (top) and angular velocity (bottom).

again an unimodal behavior, with maximum again near the mean value. But now a large dispersion around the mean can be seen.

Moreover, in Figure 33 it is shown the nominal model, the mean value, and the 95% probability envelope of beam transversal displacement and velocity in z at $x = 50\ m$. Here the mean values of both, velocity and displacement, present correlation with the nominal models. Indeed, both present discrepancies in the oscillation amplitudes, especially the velocity, that are more pronounced, as before, in the instants wherein the system is subject to impacts. The confidence bands present meaningful amplitudes, what evidentiates a certain level of dispersion around the means, which are more significant, as expected, at the instants of impact.

The PDF of drilling process efficiency function is shown in Figure 34. One can observe a unimodal distribution with the maximum around 16% and wide disper-

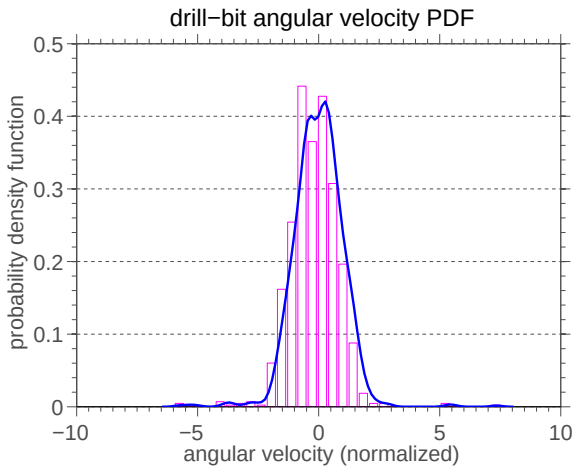

Fig. 32 Illustration of the normalized probability density function of drill-bit angular velocity.

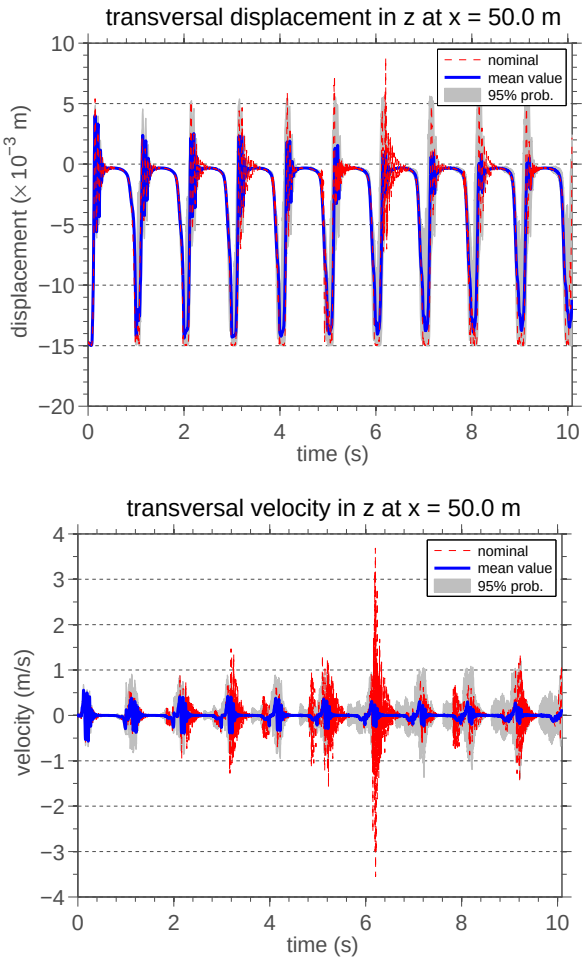

Fig. 33 Illustration of the nominal model (red line), the mean value (blue line), and the 95% probability envelope (grey shadow) for the beam transversal displacement (top) and velocity in z (bottom) at $x = 50\ m$.

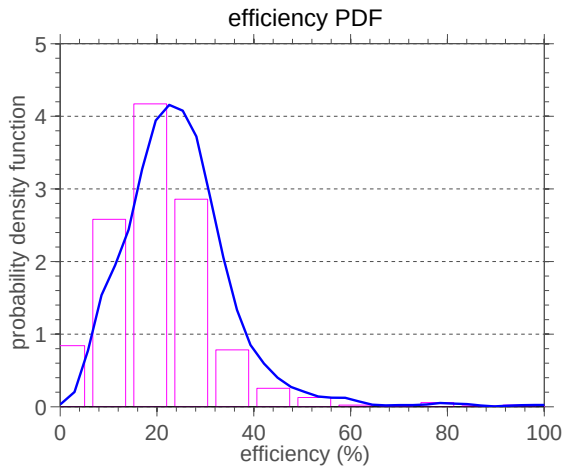

Fig. 34 Illustration of the probability density function of the drilling process efficiency.

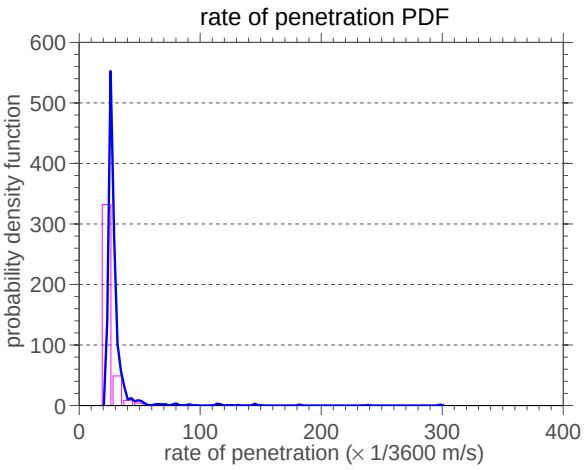

Fig. 35 Illustration of the probability density function of the rate of penetration function.

sion between 0 and 40%, declining rapidly to negligible values outside this range.

Finally, in Figure 35 one can see the PDF of drillstring rate of penetration function. One notes an unimodal behavior in a narrow range between 20 and 50 "meters per hour", with the maximum around 30 "meters per hour".

6.12 Robust optimization of drillstring rate of penetration

To improve the level of confidence of drilling process optimization, uncertainties intrinsic to the problem should be taken into account. This leads to a robust optimization problem, i.e, optimization under uncertainty where the range of random parameters are known, but not necessarily their distribution [4, 51, 7, 6, 8, 58, 3].

Taking into account the uncertainties, through the parametric approach presented in section 5, drill-bit velocity becomes the stochastic process $\mathbb{U}_{bit}(t,\theta)$, so that the random rate of penetration is defined by

$$\mathbb{ROP}(V_0,\,\Omega,\theta) = \frac{1}{t_f - t_0}\int_{t=t_0}^{t_f} \dot{\mathbb{U}}^{+}_{bit}(t,\theta)\,dt. \tag{102}$$

In the robust optimization problem, who plays the role of objective function is the expected value of the random variable $\mathbb{ROP}(V_0,\,\Omega,\theta)$, i.e., $\mathbb{E}\left[\mathbb{ROP}(V_0,\,\Omega,\theta)\right]$.

Regarding the restriction imposed by the von Mises criteria, now the equivalent stress is the random field $\sigma_{VM}(V_0,\,\Omega,\,x,\,t,\theta)$, so that the inequality is written as

$$\texttt{UTS} - \max_{\substack{0\le x\le L\\ t_0\le t\le t_f}} \left\{\sigma_{VM}(V_0,\,\Omega,\,x,\,t,\theta)\right\} \ge 0. \tag{103}$$

However, the robust optimization problem considers as restriction a probability of the event defined by inequality (103),

$$\mathbb{P}\left\{\texttt{UTS} - \max_{\substack{0\le x\le L\\ t_0\le t\le t_f}} \left\{\sigma_{VM}(V_0,\,\Omega,\,x,\,t,\theta)\right\} \ge 0\right\} \ge 1 - P_{risk}, \tag{104}$$

where $0 < P_{risk} < 1$ is the risk percentage acceptable to the problem.

A robust optimization problem very similar to this one, in the context of a vertical drillstring dynamics, is considered in [42].

To solve this robust optimization problem it is employed a trial strategy which discretizes the "operating window" in a structured grid of points and then evaluates the objective function $\mathbb{E}\left[\mathbb{ROP}(V_0,\,\Omega,\theta)\right]$ and the probabilistic constraint (104) in these points.

Accordingly, it is considered the same "operating window" used in the deterministic optimization problem solved above, i.e., $1/360\ m/s \le V_0 \le 1/90\ m/s$ and $3\pi/2\ rad/s \le \Omega \le 7\pi/3\ rad/s$, in addition to $\texttt{UTS} = 650\times 10^6\ Pa$ and $P_{risk} = 10\%$. Each MC simulation in this case used 128 realizations to compute the propagation of uncertainties.

Concerning the simulation results, the probabilistic constraint (104) is respected in all grid points that discretize the "operating window". Thus, the admissible region of robust optimization problem is equal to the "operating window". In what follows, the contour map of function $\mathbb{E}\left[\mathbb{ROP}(V_0,\,\Omega,\theta)\right]$ can be see in Figure 36. Note that the maximum, which is indicated on the graph with a blue cross, occurs at the point

$(V_0, \Omega) = (1/90\ m/s, 7\pi/3\ rad/s)$. This point is located in the boundary of the admissible region, in the upper right corner, and corresponds to a expected value of the mean rate of penetration, during the time interval analyzed, approximately equal to 58 "meters per hour".

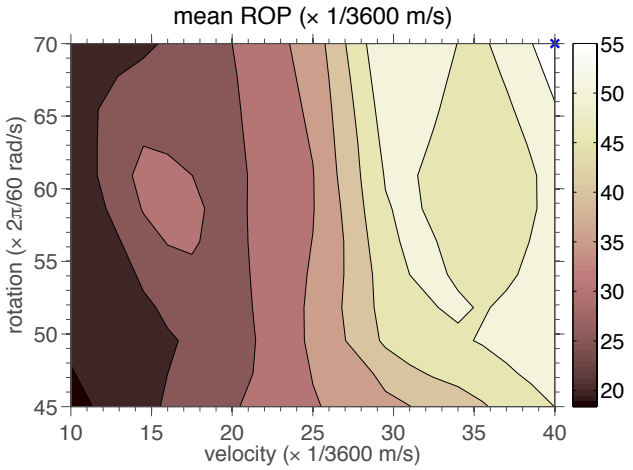

Fig. 36 Illustration of the contour plot of the mean rate of penetration function, for an "operating window" defined by $1/360\ m/s \leq V_0 \leq 1/90\ m/s$ and $3\pi/2\ rad/s \leq \Omega \leq 7\pi/3\ rad/s$. The maximum is indicated with a blue cross in the upper right corner.

This result says that, in the "operating window" considered here, increasing drillstring rotational and translational velocities provides the most robust strategy to maximize its ROP into the soil. This is in some ways an intuitive result, but is at odds with the result of the deterministic optimization problem, which provides another strategy to achieve optimum operating condition.

7 Concluding remarks

A model was developed in this work to describe the nonlinear dynamics of horizontal drillstrings. The model uses a beam theory, with effects of rotatory inertia and shear deformation, which is capable of reproducing large displacements that the beam undergoes. This model also considers the friction and shock effects due to transversal impacts, as well as, the force and torque induced by bit-rock interaction.

It should be emphasized that the paper not only proposes a mechanical analysis of this complex dynamic system, but, through this analysis, also provides a formulation for this type of system, and a methodology, that can be reused to other rotating slender mechanical systems subjected to friction and shock effects.

Numerical simulations showed that the mechanical system of interest has a very rich nonlinear dynamics, which reproduces complex phenomena such as bit-bounce, stick-slip, and transverse impacts. The study also indicated that large velocity fluctuations observed in the phenomena of bit-bounce and stick-slip are correlated with the transverse impacts, i.e., with the number of shocks per unit time which the system is subjected. Also, the mechanical impacts cause the beam to assume complex spatial configurations, which are formed by flexural modes associated to high natural frequencies.

A study aiming to maximize drilling process efficiency, varying drillstring velocities of translation and rotation was presented. The optimization strategy used a trial approach to seek for a local maximum, which was located within "operating window" and corresponds to an efficiency of approximately 16%.

The probabilistic analysis of the nonlinear dynamics showed that, with respect to the velocities, nominal model and mean value of the stochastic model differ significantly. Furthermore, at the instants which the system was subjected to mechanical impacts, it was possible to see a more pronounced dispersion around the mean value. Regarding the velocities probability distributions, it was noticed a unimodal behavior essentially.

Two optimizations problems, one deterministic and one robust, where the objective was to maximize drillstring rate of penetration into the soil, respecting its structural limits, were formulated and solved. The solutions of these problems provided two different strategies to optimize the ROP.

Finally, it sounds stressing that the mathematical model used in this work has not gone through any process of experimental validation. This is because experimental data for this type of system is difficult to be obtained, and to construct an experimental apparatus in real scale is virtually impossible. An interesting proposal for future work would be the construction of an experimental test rig, in reduced scale, that emulates the main aspects of a real drillstring. The model used in this study could be validated, following, for instance, the methodology presented in [1], with the aid of experimental measurements taken from this reduced apparatus.

A Geometric nonlinearly force coefficients

This appendix presents the coefficients which appears in geometric nonlinearity force of Eq.(49). For the sake of saving space, in the following lines it is used the abbreviations: $S_{\theta_x} = \sin\theta_x$, and $C_{\theta_x} = \cos\theta_x$.

$$\begin{aligned}\Gamma_1 = {} & E\,I_4\,(1+u')\left(v'\,\theta'_y + w'\,\theta'_z\right)S_{\theta_x}\,\theta'_x \;+ \\ & E\,I_4\,(1+u')\left(v'\,\theta'_z - w'\,\theta'_y\right)C_{\theta_x}\,\theta'_x \;+ \\ & k_s\,G\,A\,(1+u')\left(\theta_z\,v' - \theta_y\,w'\right)S_{\theta_x} \;- \\ & k_s\,G\,A\,(1+u')\left(\theta_y\,v' + \theta_z\,w'\right)C_{\theta_x},\end{aligned} \tag{105}$$

$$\begin{aligned}\Gamma_2 = {} & k_s\,G\,I_4\left(\theta_y\left(\theta'^{\,2}_y + \theta'^{\,2}_z\right) - \theta'_x\,\theta'_z\right) \;+ \\ & k_s\,G\,A\left(-w' + u'\,\theta_y\,(2+u')\right) \;- \\ & k_s\,G\,A\,(1+u')\left(v'\,S_{\theta_x} - w'\,C_{\theta_x}\right),\end{aligned} \tag{106}$$

$$\begin{aligned}\Gamma_3 = {} & k_s\,G\,I_4\left(\theta_z\left(\theta'^{\,2}_y + \theta'^{\,2}_z\right) + \theta'_x\,\theta'_y\right) \;+ \\ & k_s\,G\,A\left(v' + u'\,\theta_z\,(2+u')\right) \;- \\ & k_s\,G\,A\,(1+u')\left(w'\,S_{\theta_x} + v'\,C_{\theta_x}\right),\end{aligned} \tag{107}$$

$$\begin{aligned}\Gamma_4 = {} & E\,A\left(\frac{1}{2}\,(1+u')\left(v'^{\,2} + w'^{\,2}\right) + \frac{1}{2}u'^{\,2}\,(3+u')\right) \;+ \\ & E\,I_4\left(S_{\theta_x}\left(v'\,\theta'_z - w'\,\theta'_y\right) - C_{\theta_x}\left(v'\,\theta'_y + w'\,\theta'_z\right)\right)\theta'_x \;+ \\ & E\,I_4\,(1+u')\left(\theta'^{\,2}_x + \frac{3}{2}\left(\theta'^{\,2}_y + \theta'^{\,2}_z\right)\right) \;+ \\ & k_s\,G\,A\left(C_{\theta_x}\left(\theta_y\,w' - \theta_z\,v'\right) - S_{\theta_x}\left(\theta_y\,v' + \theta_z\,w'\right)\right) \;+ \\ & k_s\,G\,A\,(1+u')\left(\theta_y^2 + \theta_z^2\right),\end{aligned} \tag{108}$$

$$\begin{aligned}\Gamma_5 = {} & E\,A\left(u' + \frac{1}{2}\left(u'^{\,2} + v'^{\,2} + w'^{\,2}\right)\right)v' \;+ \\ & E\,I_4\left(2\,\theta'^{\,2}_x + \frac{1}{2}\left(\theta'^{\,2}_y + \theta'^{\,2}_z\right)\right)v' \;+ \\ & E\,I_4\,(1+u')\left(\theta'_z S_{\theta_x} - \theta'_y C_{\theta_x}\right)\theta'_x \;+ \\ & k_s\,G\,A\,(1+u')\left(\theta_z - \theta_y\,S_{\theta_x} - \theta_z\,C_{\theta_x}\right),\end{aligned} \tag{109}$$

$$\begin{aligned}\Gamma_6 = {} & E\,A\left(u' + \frac{1}{2}\left(u'^{\,2} + v'^{\,2} + w'^{\,2}\right)\right)w' \;+ \\ & E\,I_4\left(2\,\theta'^{\,2}_x + \frac{1}{2}\left(\theta'^{\,2}_y + \theta'^{\,2}_z\right)\right)w' \;+ \\ & E\,I_4\,(1+u')\left(-\theta'_y\,S_{\theta_x} - \theta'_z\,C_{\theta_x}\right)\theta'_x \;+ \\ & k_s\,G\,A\,(1+u')\left(-\theta_y + \theta_y\,C_{\theta_x} - \theta_z\,S_{\theta_x}\right),\end{aligned} \tag{110}$$

$$\begin{aligned}\Gamma_7 = {} & E\,I_4\left(u'^{\,2} + 2\left(u' + v'^{\,2} + w'^{\,2}\right)\right)\theta'_x \;+ \\ & E\,I_4\,(1+u')\left(v'\,\theta'_z - w'\,\theta'_y\right)S_{\theta_x} \;- \\ & E\,I_4\,(1+u')\left(v'\,\theta'_y + w'\,\theta'_z\right)C_{\theta_x} \;+ \\ & E\,I_6\left(4\,\theta'^{\,2}_x + 2\left(\theta'^{\,2}_y + \theta'^{\,2}_z\right)\right)\theta'_x \;+ \\ & k_s\,G\,A\left(\theta_z\,\theta'_y - \theta_y\,\theta'_z\right),\end{aligned} \tag{111}$$

$$\begin{aligned}\Gamma_8 = {} & E\,I_4\left(3\,u' + \frac{1}{2}\left(3\,u'^{\,2} + v'^{\,2} + w'^{\,2}\right)\right)\theta'_y \;+ \\ & E\,I_4\,(1+u')\left(-w'\,S_{\theta_x} - v'\,C_{\theta_x}\right)\theta'_x \;+ \\ & E\,I_6\left(2\,\theta'^{\,2}_x + \frac{3}{2}\left(\theta'^{\,2}_y + \theta'^{\,2}_z\right)\right)\theta'_y \;+ \\ & k_s\,G\,I_4\left(\theta_z\,\theta'_x + \theta'_y\left(\theta_y^2 + \theta_z^2\right)\right),\end{aligned} \tag{112}$$

and

$$\begin{aligned}\Gamma_9 = {} & E\,I_4\left(3\,u' + \frac{1}{2}\left(3\,u'^{\,2} + v'^{\,2} + w'^{\,2}\right)\right)\theta'_z \;+ \\ & E\,I_4\,(1+u')\left(v'\,S_{\theta_x} - w'\,C_{\theta_x}\right)\theta'_x \;+ \\ & E\,I_6\left(2\theta'^{\,2}_x + \frac{3}{2}\left(\theta'^{\,2}_y + \theta'^{\,2}_z\right)\right)\theta'_z \;+ \\ & k_s\,G\,I_4\left(-\theta_y\,\theta'_x + \theta'_z\left(\theta_y^2 + \theta_z^2\right)\right).\end{aligned} \tag{113}$$

Acknowledgements The authors are indebted to Brazilian agencies CNPq, CAPES, and FAPERJ, and French agency COFECUB for the financial support given to this research. The first author is grateful for the institutional support received from PUC-Rio and Université Paris-Est to carry out this work.

References

1. Batou A, Soize C (2009) Identification of stochastic loads applied to a non-linear dynamical system using an uncertain computational model and experimental responses. Computational Mechanics 43:559–571, DOI 10.1007/s00466-008-0330-y
2. Bazoune A, Khulief YA, Stephen NG (2003) Shape functions of three-dimensional Timoshenko beam element. Journal of Sound and Vibration 259:473–480, DOI 10.1006/jsvi.2002.5122
3. Ben-Tal A, Ghaoui LE, Nemirovski A (2009) Robust Optimization. Princeton University Press, Princeton
4. Beyer HG, Sendhoff B (2007) Robust optimization – A comprehensive survey. Computer Methods in Applied Mechanics and Engineering 196:3190–3218, DOI 10.1016/j.cma.2007.03.003
5. Bonet J, Wood RD (2008) Nonlinear Continuum Mechanics for Finite Element Analysis, 2nd edn. Cambridge University Press, Cambridge
6. Capiez-Lernout E, Soize C (2008) Design optimization with an uncertain vibroacoustic model. Journal of Vibration and Acoustics 130:021,001, DOI 10.1115/1.2827988
7. Capiez-Lernout E, Soize C (2008) Robust design optimization in computational mechanics. Journal of Applied Mechanics 75:021,001, DOI 10.1115/1.2775493
8. Capiez-Lernout E, Soize C (2008) Robust updating of uncertain damping models in structural dynamics for low- and medium-frequency ranges. Mechanical Systems and Signal Processing 22:1774–1792, DOI 10.1016/j.ymssp.2008.02.005
9. Chatjigeorgiou IK (2013) Numerical simulation of the chaotic lateral vibrations of long rotating beams. Applied Mathematics and Computation 219:5592–5612, DOI 10.1016/j.amc.2012.11.076

10. Chevallier A (2000) Nonlinear Stochastic Drilling Vibrations. Ph.D Thesis, Rice University, Houston
11. Cull SJ, Tucker RW (1999) On the modelling of Coulomb friction. Journal of Physics A: Mathematical and General 32:2103–2113, DOI 10.1088/0305-4470/32/11/006
12. Cunha Jr A (2015) Modeling and Uncertainty Quantification in the Nonlinear Stochastic Dynamics of a Horizontal Dsrillstrings. D.Sc. Thesis, Pontifícia Universidade Católica do Rio de Janeiro / Université Paris-Est
13. Cunha Jr A, Nasser R, Sampaio R, Lopes H, Breitman K (2014) Uncertainty quantification through Monte Carlo method in a cloud computing setting. Computer Physics Communications 185:1355—1363, DOI 10.1016/j.cpc.2014.01.006, DOI 10.1016/j.cpc.2014.01.006
14. Davies RJ, Almond S, Ward RS, Jackson RB, Adams C, Worrall F, Herringshaw LG, Gluyas JG, Whitehead MA (in press) Oil and gas wells and their integrity: Implications for shale and unconventional resource exploitation. Marine and Petroleum Geology DOI http://dx.doi.org/10.1016/j.marpetgeo.2014.03.001
15. Depouhon A, Detournay E (2014) Instability regimes and self-excited vibrations in deep drilling systems. Journal of Sound and Vibration 333:2019–2039, DOI 10.1016/j.jsv.2013.10.005
16. Detournay E, Richard T, Shepherd M (2008) Drilling response of drag bits: Theory and experiment. International Journal of Rock Mechanics & Mining Sciences 45:1347–1360, DOI 10.1016/j.ijrmms.2008.01.010
17. Divenyi S, Savi MA, Wiercigroch M, Pavlovskaia E (2012) Drill-string vibration analysis using non-smooth dynamics approach. Nonlinear Dynamics 70:1017–1035, DOI 10.1007/s11071-012-0510-3
18. Franca LFP (2010) Drilling action of roller-cone bits: modeling and experimental validation. Journal of Energy Resources Technology 132:043,101–1–043,101–9, DOI 10.1115/1.4003168
19. Franca LFP, Weber HI (2004) Experimental and numerical study of a new resonance hammer drilling model with drift. Chaos, Solitons & Fractals 21:789–801, DOI 10.1016/j.chaos.2003.12.064
20. Freudenrich C, Strickland J (2001) How Oil Drilling Works. http://www.howstuffworks.com/oil-drilling
21. Gilardi G, Sharf I (2002) Literature survey of contact dynamics modelling. Mechanism and Machine Theory 37:1213–1239, DOI 10.1016/S0094-114X(02)00045-9
22. Golub GH, Van Loan CF (2013) Matrix Computations, 4th edn. The Johns Hopkins University Press, Baltimore
23. Hagedorn P, DasGupta A (2007) Vibrations and Waves in Continuous Mechanical Systems. Wiley, Chichester
24. Hu Y, Di Q, Zhu W, Chen Z, Wang W (2012) Dynamic characteristics analysis of drillstring in the ultra-deep well with spatial curved beam finite element. Journal of Petroleum Science and Engineering 82—83:166–173, DOI 10.1016/j.petrol.2012.01.011
25. Hughes TJR (2000) The Finite Element Method. Dover Publications, New York
26. Hunt KH, Crossley FE (1975) Coefficient of restitution interpreted as damping in vibroimpact. Journal of Applied Mechanics 42:440–445, DOI 10.1115/1.3423596
27. Jansen JD (1993) Nonlinear Dynamics of Oilwell Drillstrings. Ph.D Thesis, TU Delft, Amsterdam
28. Khulief YA, Al-Sulaiman FA, Bashmal S (2007) Vibration analysis of drillstrings with self-excited stick–slip oscillations. Journal of Sound and Vibration 299:540–558, DOI 10.1016/j.jsv.2006.06.065
29. Kroese DP, Taimre T, Botev ZI (2011) Handbook of Monte Carlo Methods. Wiley, New Jersey
30. Lanczos C (1986) The Variational Principles of Mechanics, 4th edn. Dover Publications, New York
31. Litewka P, Wriggers P (2002) Frictional contact between 3D beams. Computational Mechanics 28:26–39, DOI 10.1007/s004660100266
32. Liu X, Vlajic N, Long X, Meng G, Balachandran B (2013) Nonlinear motions of a flexible rotor with a drill bit: stick-slip and delay effects. Nonlinear Dynamics 72:61–77, DOI 10.1007/s11071-012-0690-x
33. Macdonald KA, Bjune JV (2007) Failure analysis of drillstrings. Engineering Failure Analysis 14:1641–1666, DOI 10.1016/j.engfailanal.2006.11.073
34. Nandakumar K, Wiercigroch M (2013) Stability analysis of a state dependent delayed, coupled two DOF model of drill-stringvibration. Journal of Sound and Vibration 332:2575–2592, DOI 10.1016/j.jsv.2012.12.020
35. Newmark NM (1959) A method of computation for structural dynamics. Journal of the Engineering Mechanics Division 85:67–94
36. Oberkampf WL, Roy CJ (2010) Verification and Validation in Scientific Computing. Cambridge University Press, Cambridge
37. Oppenheim AV, Schafer RW (2009) Discrete-Time Signal Processing, 3rd edn. Prentice Hall, Englewood Cliffs, N.J.
38. Reddy JN (1997) On locking-free shear deformable beam finite elements. Computer Methods in Applied Mechanics and Engineering 149:113–132, DOI 10.1016/S0045-7825(97)00075-3
39. Ritto TG (2010) Numerical Analysis of the Nonlinear Dynamics of a Drill-string with Uncertainty Modeling. D.Sc. Thesis, Pontifícia Universidade Católica do Rio de Janeiro / Université Paris-Est
40. Ritto TG, Sampaio R (2012) Stochastic drill-string dynamics with uncertainty on the imposed speed and on the bit-rock parameters. International Journal for Uncertainty Quantification 2:111–124, DOI 10.1615/Int.J.UncertaintyQuantification.v2.i2
41. Ritto TG, Soize C, Sampaio R (2009) Non-linear dynamics of a drill-string with uncertain model of the bit–rock interaction. International Journal of Non-Linear Mechanics 44:865–876, DOI 10.1016/j.ijnonlinmec.2009.06.003
42. Ritto TG, Soize C, Sampaio R (2010) Robust optimization of the rate of penetration of a drill-string using a stochastic nonlinear dynamical model. Computational Mechanics 45:415–427, DOI 10.1007/s00466-009-0462-8
43. Ritto TG, Soize C, Sampaio R (2010) Stochastic dynamics of a drill-string with uncertain weight-on-hook. Journal of the Brazilian Society of Mechanical Sciences and Engineering 32:250–258, DOI 10.1590/S1678-58782010000300008
44. Ritto TG, Escalante MR, Sampaio R, Rosales MB (2013) Drill-string horizontal dynamics with uncertainty on the frictional force. Journal of Sound and Vibration 332:145–153, DOI 10.1016/j.jsv.2012.08.007
45. Sagan H (1992) Introduction to the Calculus of Variations. Dover Publications, New York
46. Sahebkar SM, Ghazavi MR, Khadem SE, Ghayesh MH (2011) Nonlinear vibration analysis of an axially moving drillstring system with time dependent axial load and axial velocity in inclined well. Mechanism and Machine Theory 46:743–760, DOI 10.1016/j.mechmachtheory.2010.12.003

47. Sampaio R, Piovan M, Lozano GV (2007) Coupled axial/torsional vibrations of drill-strings by means of non-linear model. Mechanics Research Communications 34:497–502, DOI 10.1016/j.mechrescom.2007.03.005
48. Savitzky A, Golay MJE (1964) Smoothing and differentiation of data by simplified least squares procedures. Analytical Chemistry 36:1627–1639, DOI 10.1021/ac60214a047
49. Schuëller GI (1997) A state-of-the-art report on computational stochastic mechanics. Probabilistic Engineering Mechanics 12:197–321, DOI 10.1016/S0266-8920(97)00003-9
50. Schuëller GI (2007) On the treatment of uncertainties in structural mechanics and analysis. Computers & Structures 85:235–243, DOI 10.1016/j.compstruc.2006.10.009
51. Schuëller GI, Jensen HA (2008) Computational methods in optimization considering uncertainties – an overview. Computer Methods in Applied Mechanics and Engineering 198:2–13, DOI 10.1016/j.cma.2008.05.004
52. Silveira M, Wiercigroch M (2009) Low dimensional models for stick-slip vibration of drill-strings. Journal of Physics: Conference Series 181:012,056, DOI 10.1088/1742-6596/181/1/012056
53. Soize C (2000) A nonparametric model of random uncertainties for reduced matrix models in structural dynamics. Probabilistic Engineering Mechanics 15:277–294, DOI 10.1016/S0266-8920(99)00028-4
54. Soize C (2001) Maximum entropy approach for modeling random uncertainties in transient elastodynamics. Journal of the Acoustical Society of America 109:1979–1996, DOI 10.1121/1.1360716
55. Soize C (2005) A comprehensive overview of a non-parametric probabilistic approach of model uncertainties for predictive models in structural dynamics. Journal of Sound and Vibration 288:623–652, DOI 10.1016/j.jsv.2005.07.009
56. Soize C (2012) Stochastic Models of Uncertainties in Computational Mechanics. Amer Society of Civil Engineers, Reston
57. Soize C (2013) Stochastic modeling of uncertainties in computational structural dynamics — recent theoretical advances. Journal of Sound and Vibration 332:2379––2395, DOI 10.1016/j.jsv.2011.10.010
58. Soize C, Capiez-Lernout E, Ohayon R (2008) Robust updating of uncertain computational models using experimental modal analysis. AIAA Journal 46:2955–2965
59. Spanos PD, Chevallier AM, Politis NP (2002) Nonlinear stochastic drill-string vibrations. Journal of Vibration and Acoustics 124:512–518, DOI 10.1115/1.1502669
60. Spanos PD, Chevallier AM, Politis NP, Payne ML (2003) Oil and gas well drilling: a vibrations perspective. The Shock and Vibration Digest 35:85–103
61. Trindade MA, Wolter C, Sampaio R (2005) Karhunen–Loève decomposition of coupled axial/bending vibrations of beams subject to impacts. Journal of Sound and Vibration 279:1015–1036, DOI 10.1016/j.jsv.2003.11.057
62. Willoughby D (2005) Horizontal Directional Drilling (HDD): Utility and Pipeline Applications. McGraw-Hill, New York
63. Wriggers P (2006) Computational Contact Mechanics, 2nd edn. Springer, New York
64. Wriggers P, Zavarise G (2004) Computational Contact Mechanics. In: Stein E, de Borst R, Hughes TJR (eds) Encyclopedia of Computational Mechanics, vol 2, Wiley, Hoboken, pp 195–226, DOI 10.1002/0470091355.ecm033
65. Wriggers P, Wagner W, Stein E (1987) Algorithms for non-linear contact constraints with application to stability problems of rods and shells. Computational Mechanics 2:215–230, DOI 10.1007/BF00571026
66. Young DM (2003) Iterative Solution of Large Linear Systems. Dover Publications, New York
67. Zhang Y, Sharf I (2009) Validation of nonlinear viscoelastic contact force models for low speed impact. Journal of Applied Mechanics 76:051,002, DOI 10.1115/1.3112739
68. Zhu X, Liu Y, Tong H (2014) Analysis of reamer failure based on vibration analysis of the rock breaking in horizontal directional drilling. Engineering Failure Analysis 37:64 – 74, DOI 10.1016/j.engfailanal.2013.11.016